Bioactive Materials 10 (2022) 378–396

Contents lists available at ScienceDirect

Bioactive Materials

journal homepage: www.sciencedirect.com/journal/bioactive-materials

Two-stage degradation and novel functional endothelium characteristics of a 3-D printed bioresorbable scaffold

Tieying Yin [a,1,*], Ruolin Du [a,1], Yang Wang [a,1], Junyang Huang [a], Shuang Ge [a], Yuhua Huang [a], Youhua Tan [b], Qing Liu [c], Zhong Chen [d], Hanqing Feng [c], Jie Du [e], Yazhou Wang [a,f,**], Guixue Wang [a,***]

[a] Key Laboratory for Biorheological Science and Technology of Ministry of Education, State and Local Joint Engineering Laboratory for Vascular Implants, Bioengineering College of Chongqing University, Chongqing, 400030, China
[b] Department of Biomedical Engineering, The Hong Kong Polytechnic University, Hong Kong SAR, China
[c] Beijing Advanced Medical Technologies Inc., Beijing, 102609, China
[d] Beijing Anzhen Hospital of Capital Medical University, Beijing, 100029, China
[e] Beijing Institute of Heart, Lung, and Blood Vessel Diseases, Beijing Anzhen Hospital, Capital Medical University, 2 Anzhen Ave, Beijing, 10029, China
[f] School of Medicine, Chongqing University, Chongqing, 400044, China

ARTICLE INFO

Keywords:
Intravascular stents
3-D printing
Bioresorbable scaffold
Degradation behavior
Functional endothelium

ABSTRACT

Bioresorbable scaffolds have emerged as a new generation of vascular implants for the treatment of atherosclerosis, and designed to provide a temporary scaffold that is subsequently absorbed by blood vessels over time. Presently, there is insufficient data on the biological and mechanical responses of blood vessels accompanied by bioresorbable scaffolds (BRS) degradation. Therefore, it is necessary to investigate the inflexion point of degradation, the response of blood vessels, and the pathophysiological process of vascular, as results of such studies will be of great value for the design of next generation of BRS. In this study, abdominal aortas of SD rats were received 3-D printed poly-*l*-actide vascular scaffolds (PLS) for various durations up to 12 months. The response of PLS implanted aorta went through two distinct processes: (1) the neointima with desirable barrier function was obtained in 1 month, accompanied with slow degradation, inflammation, and intimal hyperplasia; (2) significant degradation occurred from 6 months, accompanied with decreasing inflammation and intimal hyperplasia, while the extracellular matrix recovered to normal vessels which indicate the positive remodeling. These *in vivo* results indicate that 6 months is a key turning point. This "two-stage degradation and vascular characteristics" is proposed to elucidate the long-term effects of PLS on vascular repair and demonstrated the potential of PLS in promoting endothelium function and positive remodeling, which highlights the benefits of PLS and shed some light in the future researches, such as drug combination coatings design.

1. Introduction

Atherosclerosis (AS) is a major cardiovascular disease which threatens the health of humans worldwide. Currently, implanting drug-eluting stent (DES) provides the most effective treatment through enlarging the lumen of an artery narrowed by an atherosclerotic lesion. However, DES implantation has several drawbacks, including the onset of late stent thrombosis, neo-atherosclerosis, and local inflammation due to the introduction of this aforementioned foreign body [1]. In an attempt at overcoming these limitations, BRS have been developed to

Peer review under responsibility of KeAi Communications Co., Ltd.

* Corresponding author. Key Laboratory for Biorheological Science and Technology of Ministry of Education, State and Local Joint Engineering Laboratory for Vascular Implants, Bioengineering College of Chongqing University, Chongqing, 400030, China.

** Corresponding author. School of medicine, Key Laboratory for Biorheological Science and Technology of Ministry of Education, State and Local Joint Engineering Laboratory for Vascular Implants, Bioengineering College of Chongqing University, Chongqing, 400030, China.

*** Corresponding author. Key Laboratory for Biorheological Science and Technology of Ministry of Education, State and Local Joint Engineering Laboratory for Vascular Implants, Bioengineering College of Chongqing University, Chongqing University, Chongqing 400044, China.

E-mail addresses: tieying_yin@cqu.edu.cn (T. Yin), yazhou_wang@cqu.edu.cn (Y. Wang), wanggx@cqu.edu.cn (G. Wang).

[1] These authors contributed equally to this work.

https://doi.org/10.1016/j.bioactmat.2021.08.020
Received 2 May 2021; Received in revised form 17 August 2021; Accepted 18 August 2021
Available online 24 August 2021

enable transient scaffolds for blood vessels and eventually disappear completely, leaving behind the native vessels close to their natural state [1,2]. Besides, BRS prevent acute vessel recoil and can briefly elute an anti-proliferative drug to counteract the constrictive remodeling. These expectations from clinicals and potentials of BRS promoted the development of the field.

Presently, poly-L-lactic acid (PLLA)- based scaffolds (e.g., MeRes100 [3]) and PLLA-based materials (e.g., DESolve [4] and NeoVas [5]) have shown promising results in preclinical animal studies as well as a few short and mid-term clinical trials. These have shown that the 1-year in-device late lumen loss ratio and the risk of stent thrombosis for Absorb, a bioresorbable vascular scaffold (BVS; Abbott Vascular, manufactured from PLLA), were similar to those of Xience, an everolimus-eluting metallic stent, whereas adverse effects were noted at 2–5 years [6–9]. Furthermore, several animal studies and clinical trials have examined the response of vessels to the degradation of BRS [10]. To further complicate matters, the precise time point of scaffold degradation remains undefined. Thus, it is important to investigate the time course of the vascular changes along with the biodegradation of the scaffold.

Recently, research on BRS has advanced rapidly in China with clinical trials now common. In one such study, it was found that biodegradable alloy based vascular implants showed minimal/moderate acute toxicity as well as favorable physiological degradation [11,12], the Xinsorb BRS is at the forefront of technological innovation [13], while Lepu Medical's NeoVas BRS has recently been approved for clinical use in China [5,14]. Further clinical trials on BVS and Xinsorb revealed acceptable target vessel-related myocardial infarction but without discussion on degradation induced phenotype and functions of vascular cells [15–17]. The implantation of AMsorb™ BRS, a 3-D printed PLLA scaffold, showed that complete reendothelializations could be achieved within 90 days with no thrombus formation [18]. Furthermore, the first AMsorb™ clinical trial is ongoing in China (Clinical Trial Protocol, Approval No. 2019L0001, National Medical Products Administration, China). In this study, PLS is implanted in the abdominal aorta of SD (Sprague Dawley) rats, with endothelial function evaluated post-implantation where vascular remodeling of the abdominal aorta is also examined. This revealed that the main inflammatory reaction occurred one week after PLS implantation while neointimal hyperplasia was extensive at one month. After 3 months full function of the neointimal barrier was recovered and reendothelialization was completed. However, the degree of vascular proliferation followed a sinusoidal waveform-like pattern, first rising before decreasing after 6 months. PLS degradation was significant 6 months post-implantation, at which point vessels began to reform.

By focusing on the temporal course of vascular remodeling, the aim of this study is to obtain new information which will bring about the design of superior drug coatings as well as more effective, e.g., anti-inflammatory drugs and intimal function- promoting drugs.

2. Experimental materials and methods

2.1. Experimental materials

After purchase from Army Medical University Animal Experiment center, 60 SD rats with a mean mass of 300g were fed on a normal diet and used in accordance with the guidelines of the Chinese Animal Care and Use Committee standards. Moreover, all procedures were approved by the Ethics Committee and Authority. PLS (Φ2.0 × 13 mm, strut thickness 150 μm) were manufactured by Beijing Advanced Medical Technologies, Ltd Inc. (Beijing, China) using a proprietary 3-D printing technology [19] and bare metal stents (BMS, Φ2.0 × 13 mm) were purchased from Beijing Amsino Medical Devices Co., Ltd. Human umbilical vein endothelial cells (HUVECs), human myeloid leukemia mononuclear cells (THP-1) and rat thoracic aorta smooth muscle cells (SMCs) were all purchased from Cell Bank of Chinese Academy of Sciences.

2.2. Methods

2.2.1. Printing and mechanical tests of PLS

To print PLS, the computer aided design model was converted into a 3D printing program and used for printing. The scaffolds were printed at a temperature 220 °C with a 150 μm nozzle on a rotation conical shaped mandrel (the 4th axis, Φ2.00 mm). Conical shaped scaffolds for testing were fabricated with a length of 13 mm, inter diameter 2.0 mm. The strut thickness is 150 μm. After the scaffolds were cooled down to room temperature, the scaffolds were removed from the mandrel.

To better understand the mechanical properties of PLS, tests to measure recoil (referred to YY/T0694-2008 ASTM F2079-02, MOD), foreshortening (referred to YY/T 0693–2008 ASTM F 2081–06, MOD) were carried out. For recoil and foreshortening, the length (L_0) of 9 PLS crimped on the balloon catheter was measured using a vernier caliper. Before dilation, the scaffolds were immersed in a water bath for 2 min with temperature kept constant at 37 °C throughout. The balloon catheter was then connected to a pressure filling pump and slowly increased the pressure from zero to 608 KPa (6 atm) over a period of 12–15 s at which point it was held constant for 30 s. The outer diameters (D_0) of the scaffolds were measured under a microscope (Motic, SMZ-171). After releasing the pressure, the scaffolds were blot dried with a dust-free cloth and examined under the same microscope with their outer diameter (D) and the length (L) of the scaffolds measured using a caliper.

The formula for calculating the foreshortening rate of scaffolds η (measured as a %) is

$$\eta = \left|\frac{L0 - L}{L0}\right| \times 100\%$$

where L (measured in mm) is the steady state length of the dilated scaffolds after pressure has been released and L_0 denotes their initial length (of the crimped scaffold on the balloon).

Similarly, the radial recoil rate of scaffolds ζ is calculated (again as a %) by

$$\zeta = \left|\frac{D0 - D}{D0}\right| \times 100\%$$

where D (measured in mm) is the outer diameter of the dilated scaffolds in the aforementioned steady state with the outer diameter given by D_0.

To measure the radial compressing force, the radial force tester (BLOCKWISE MODEL TTR2) (Fig. S1) was preheated for approximately 30 min until a temperature of 37 °C was reached. In total, nine PLS were compressed along the radial direction in the crimping chamber, this was carried out at a speed of 0.5 mm/s and stopped when the diameter reached 1.5 mm with the radial strength-deformation curve then recorded (Software: Radial Force, edition: 2.4.3). Scaffold radial strength is defined as the maximum radial strength within the range from 0 to 15% of the radial deformation of the scaffold. The strength-rebounding curve was subsequently obtained when the crimping chamber was opened at a speed of 0.5 mm/s due to the rebound of the compressed scaffold.

To measure molecular weight of the material, the gel permeation chromatography (GPC, WATERS MODEL 1525-2414-2707) was used. The column temperature was set and held constant at 35 °C, the mobile phase was trichloromethane (Quzhou Huafu Refrirerant New material CO., Ltd. China, CAS: 67-66-3), flow rate was 1 mL/min and the detector was a parallax refractive index detector. Initially, a 10 mg scaffold was dissolved into 1 mL trichloromethane by leaving immersed for a minimum of 12 h, after which the sample solution was filtrated using a 0.22 μm microporous filter. The filtrated solution of 20 μL was then accurately injected into the GPC in order to determine the molecular weight of the scaffold material.

2.2.2. Implantation and explanation of BMS and PLLA scaffolds

Of the sixty adult SD rats which were purchased, thirty were successfully implanted with BMS and thirty with PLS. Three days before this procedure, Aspirin (Bayer, 10 mg/kg/day) and Clopidogrel (Lepu Pharmaceuticals, Inc., 7.5 mg/kg/day) regimens were started and continued until sacrifice. During implantation, a PLS or BMS, was deployed in the abdominal aortas of SD rats, with ~2 mm diameter. To do this, the abdominal aortas and iliac arteries were surgically exposed and blood flow temporarily blocked from the proximal end of the abdominal aorta to the distal end of the iliac artery. A 1/3 (relatively distance of right iliac artery to abdominal aorta) vascular incision in the right iliac artery was opened and then the scaffolds crimped onto balloon catheters which were positioned in the abdominal aorta. These balloons (Φ 2.0 × 15 mm) were then inflated with 8 atm for 30 s at which point the scaffolds were deployed and balloons removed post deflation. The proximal end of the right iliac artery remained blocked while flow was unblocked in the abdominal aorta and left iliac artery before the vascular incision was sutured and all blood flow blockage was removed.

Additionally, due to water absorption of PLS, implantation of PLS was carried out in a timely and efficient manner. The arteries contained the scaffolds and main organs of the rats were harvested for subsequent analysis. Meanwhile, blood samples were collected for blood routine and biochemical analysis.

Considering following tests and experiments, the sacrificed animals implanted with PLS or BMS in detail are in the following Table 1.

2.2.3. Evans blue staining

Post BMS or PLS implantation, ≥ three healthy SD rats were randomly selected and respectively anesthetized for periods of 1 week and 1, 3 months. The first involved a 10% chloral hydrate (Macklin, CAS: 302-17-0) by intraperitoneal injection, and then a 1 mL 2% Evans blue (Solarbio, CAS: 314-13-6) was injected by tail intravenous injection. These rats were subsequently sacrificed 1 h after the dyeing cycle at which point the heart was perfused with 0.9% saline containing one heparin sodium salt (Solarbio, CAS: 9041-08-1). At this time, blood vessels with implanted scaffolds were removed. After removing excess tissue fat, blood vessels were dissected longitudinally, fixed with 4% paraformaldehyde (Servicebio, lot: G1101-500 ML). Subsequently, these blood vessels were stored at 4 °C to be used for collecting images of the endocardium coloration.

2.2.4. Enface immunofluorescence

Evans blue stained samples washed 3 times with PBS (Servicebio, lot: G0002-2L) for 15 min each, then blocked with 1% bovine serum albumin (Solarbio, CAS:9048-46-8) and 0.3% Triton X-100 (Solarbio, CAS: 9002-93-1) in a blocking solution (PBS) for 1 h at room temperature. The samples were co-stained in mice monoclonal antibody VE-CAD (sc-52751, Santa Cruz Biotechnology, 1:200 dilution) and β-catenin rabbit polyclonal antibody (ab32572, Abcam, 1:200 dilution); mouse monoclonal antibody p120 (1:200, Santa Cruz Biotechnology), mouse monoclonal antibody ZO-1 (Cat: 33–9100, ThermoFisher Scientific, 1:100 dilution) and sheep polyclonal antibody vWF (GTX74137, GeneTex,1:200 dilution); mouse monoclonal antibody TM (sc-271804, Santa Cruz Biotechnology, 1:200 dilution), mouse monoclonal antibody ZO-1 (Cat: 33–9100, ThermoFisher Scientific, 1:100 dilution) and sheep polyclonal antibody vWF (GTX74137, GeneTex, 1:200 dilution), respectively, and incubated overnight in a wet box. Subsequently, primary antibodies were recovered, goat anti-mouse IgG H&L (ab150113, Abcam, Alexa Fluor® 488, 1:200 dilution), goat anti-donkey IgG H&L (SA00008-3, Proteintech, Alexa Fluor® 550, 1:100 dilution) and donkey anti-rabbit IgG H&L (ab150075, Abcam, Alexa Fluor® 647, 1:200 dilution) were chosen based on first antibodies (origin and species), added, and incubated for 1 h at room temperature, secondary antibody recovered, washed for 3 times with PBS for 15 min each. Following DAPI (Solarbio, CAS: 28718-90-3) stained for the inner membrane for 15 min at room temperature, samples were washed for 3 times with PBS for 15 min each. Then endothelium of the samples was placed face up on the surface of the slide and the anti-fluorescence quenching agent (Solarbio, CAS: S2100) was added. Carefully covered samples with cover slips and then pressed the coverslips to flatten the blood vessels. The images were acquired using a Leica SP8 confocal microscope (SP8, Leica, Switzerland).

Table 1
Animal grouping and sacrifice information at temporal points.

Sacrificed Temporal Points	Amount of Sacrificed Animal	
	PLS	BMS
1 week	7	8
1 month	8	6
3 months	6	6
6 months	5	6
12 months	5	3

2.2.5. Scanning electron microscope (SEM) analysis

Vessels which were implanted with BMS or PLS were, as indicated previously, removed after 1 week or 1, 3, 6, 12 months at which point they were fixed with 2.5% glutaraldehyde (Hefei TNJ Chemical Industry Co., Ltd. China, CAS: 111-30-8) and left for 12 h. Subsequently these were dehydrated using a series of gradient solutions of 30%, 50%, 70%, 80%, 90%, 100%, and 100% *tert*-butyl alcohol (Jinan Finer Chemical Co., Ltd. China, CAS: 75-65-0) with each step lasting 15 min.

Subsequently, samples were stored for 1 h in a freezer of temperature −20 °C before being freeze-dried for 12 h in an FD-1-50 freeze dryer (Boyikang Laboratory Instrument Co., Ltd. Beijing, China). The targeted artery segments were then longitudinally bisected to expose the lumen surface at which point they were coated with a thin layer of gold, by means of a polaron sputtering. SEM was performed with a Hitachi S–3700 N, this was operated at 10–15 kV to examine the endothelialization of the implanted artery lumen surfaces.

2.2.6. Doppler ultrasonography

To detect blood patency of SD rats which received PLS or BMS, Doppler ultrasonography (zoncare-V7, Feibo Medical, Wuhan, China) was applied after 1 week and 1-, 3-, and 6-months post PLS implantation. These images were subsequently processed and analyzed.

2.2.7. Optical coherence tomography (OCT) observation

Samples (after the same scaffold implantation of 1 week, 1 month, and 3, 6, 12 months) were fixed for 24 h with 4% paraformaldehyde and scanned using OCT (C7 System, St Jude Medical, St Paul, MN). Both the occlusion balloon catheter and guide wire were sent to the proximal and distal end of the scaffold/stent vessel. Normal saline solution (0.9% saline) was subsequently used to flush the vessel. At this time, the aforementioned guide wire was carefully withdrawn at a speed of 20 mm/s. The scaffold/stent segment was scanned and analyzed at consecutive intervals of 1 mm as was thrombosis. The area of scaffold and lumen area was measured to calculate the neointimal area and neointima coverage.

2.2.8. Electrolysis of BMS

Before histological analysis, BMS was electrolyzed using the previous published protocol [20]. In summary, this involves fixing vessels with 4% paraformaldehyde and immersed in a solution composed of 100 mL citric acid (Absin, Cat: abs47000808) and 5 g sodium chloride (Absin, Cat: abs42027444). The metal was dissolved by wire connecting to a 5-V power supply.

2.2.9. Histological analysis

The segments of artery which contained the scaffold/stent at each time point (1 week and 1, 3, 6, 12 months) were fixed with 4%

paraformaldehyde. Metallic stents in the BMS group were rapidly dissolved using the electrochemical method previously described. Samples were embedded in paraffin and sliced into 5 μm sections. These were then stained with hematoxylin-eosin (HE), Masson's trichrome (collagen), Verhoeff-Van Gieson (elastin), EVG (elastic fibers), Movat (nucleus, cytoplasm, collagen tissue, elastic tissue, proteoglycan), Sirius Red (type I and III collagen), and Alcian Blue with each of these stages carried out according to protocols provided by the manufacturers. For image acquisition, sections stained with HE, Masson, Verhoeff-Van Gieson, EVG, Movat, and Alcian Blue were viewed using an Olympus microscope, scanned by Case Viewer, and analyzed by Image J while sections stained with Sirius Red were observed using a polarized light microscope (NIKON Eclipse Ci).

To evaluate restoration times of endothelial barrier function, antibodies anti-CD31 (GB13248, ServiceBio, 1:3000 dilution) and anti-alpha smooth muscle actin primary antibody (GB13044, ServiceBio, 1:2000 dilution), second antibodies used were HRP-labeled with same species. To visualize macrophages, anti-CD68 antibody (ab31630, Abcam, 1:200 dilution) and anti-CD11b antibody (ab133357, Abcam, 1:200 dilution) were co-stained for immune- fluorescent staining, the second antibodies used were goat anti-mouse IgG H&L (ab150113, Abcam, Alexa Fluor® 488, 1:200 dilution) and donkey anti-rabbit IgG H&L (ab150075, Abcam, Alexa Fluor® 647, 1:200 dilution), while the numbers of macrophages in per strut was calculated using at least three stented segments at corresponding time point.

To better elucidate contribution of M2 macrophage in inflammation, anti-CD68 (ab31630, Abcam, 1:200 dilution) and anti-CD206 (M2 marker, Cat:18704-1-AP, Proteintech, 1:200 dilution), anti-CD68 (ab31630, Abcam, 1:200 dilution) and anti-CD197 (M1 marker, Cat: 25898-1-AP, Proteintech, 1:200 dilution) were co-stained at indicated time, and second antibodies used were goat anti-mouse IgG H&L (ab150113, Abcam, Alexa Fluor® 488, 1:200 dilution) and donkey anti-rabbit IgG H&L (ab150075, Abcam, Alexa Fluor® 647, 1:200 dilution), respectively.

To observe the mechanical response of blood vessels to degradation, *anti*-MGF antibody (07–2108, Merckmillipore, 1:250 dilution) and BMP2 (ab6285, Abcam, 1:200 dilution) were co-stained using immunofluorescent staining, carried out at the aforementioned times, and second antibodies that were used were goat anti-mouse IgG H&L (ab150113, Abcam, Alexa Fluor® 488, 1:200 dilution) and donkey anti-rabbit IgG H&L (ab150075, Abcam, Alexa Fluor® 647, 1:200 dilution). To observe phenotypic modulation of vascular cells during degradation, antibodies *anti*-vimentin (10366-1-AP, Ptoteintech, 1:200 dilution)/SM-MHC (NBP2-45169, Novus Biologicals, 1:200 dilution) were also co-stained at the aforementioned times, and second antibodies used in each co-stained combination were goat anti-mouse IgG H&L (ab150113, Abcam, Alexa Fluor® 488, 1:200 dilution) and donkey anti-rabbit IgG H&L (ab150075, Abcam, Alexa Fluor® 647, 1:200 dilution). Histological slides were scanned using a Panoramic 250 Digital Pathology system (3D HISTECH) and subsequently analyzed using Case Viewer software (3D HISTECH). For immuno-fluorescent observation, confocal microscopy was used. For each implantation point investigated, the internal organs were taken and fixed by 4% paraformaldehyde and then paraffin-embedded.

2.2.10. Culture of HUVECs, THP-1, SMCs, and mechanical stimulations of HUVECs and SMCs

HUVECs cultured with RPMI-1640, THP-1 and SMCs were cultured with DMEM, contained 10% Fetal Bovine Serum (FBS, Wisent Bioproduction, Cat: 086–150) in a 5% CO_2, 37 °C incubator, respectively. At confluence, to verify the inflammatory effects of PLS on SMCs, three macrophage phenotypes (M0, M1, and M2) were induced by THP-1 cells, and co-cultured with SMCs via transwell (Costar, Corning, Cat:3414). For mechanical stimulations, HUVECs were exposed to 6 dyne/cm^2 and 12 dyne/cm^2 shear stress for 6 h by a parallel plate flow chamber (Beijing Aerospace University), and SMCs were loaded with a periodic tension (10%, 1 Hz) for 12 h by Flexcell 4000 T (Flexcell International, USA).

2.2.11. Cell immuno-fluorescence staining

Following mechanical stimulations, cells were fixed with 4% paraformaldehyde, washed 3 times with PBS for 15 min each, blocked with 1% bovine serum albumin and 0.3% Triton X-100 in a blocking solution (PBS) for 1 h at room temperature. The samples were immersed in the antibody against MGF (07–2108, Merckmillipore, 1:200 dilution) and incubated overnight in a wet box. Subsequently, after primary antibodies were recovered, goat anti-mouse IgG H&L (ab150113, Abcam, Alexa Fluor® 488, 1:200 dilution) was added and incubated for a further 1 h, again at room temperature. After secondary antibody was recovered, samples were washed for 3 times with PBS for 15 min each. Then phalloidin labeled F-actin (A30106, Alexa Fluor-actin (A301Phalloidin, Thermo Fisher Scientific, 1:400 dilution) was added and incubated for 1 h at room temperature, washed for 3 times with PBS for 15 min each. Following phalloidin staining, DAPI staining 15 min at room temperature, samples were washed for 3 times with PBS for 15 min each, added anti-fluorescence quenching agent (S2100, Solarbio, Beijing) and stored at 4 °C. The images were obtained using a Leica SP8 confocal microscope.

2.2.12. Statistical analysis

The mean values ± standard deviation was calculated and plotted using GraphPad Prism 6 software while the Shapiro-Wilk test was used when analyzing data distribution. Additionally, student's t-test was applied for two groups. Differences in multiple groups with one variable were determined using one-way ANOVA while for differences in multiple groups with more than one variable, two-way ANOVA was applied. During these tests, $^*P < 0.05$ was considered to be statistically significant.

Overall, all the important events after implantation of PLS, and corresponding experiments were presented in the following illustrator (Fig. 1).

3. Results

3.1. The 3-D printed PLS possesses fine mechanical properties

Due to its function in vascular implants, the mechanical properties of endovascular scaffold are crucial. As such, nine PLS were tested *in vitro* to obtain a better understanding of these mechanical properties. It was found that the radial recoiling rate of the PLS was 2.6% ± 2.6% (Fig. 2A), even lower than Xinsorb with 0.66 ± 4.32% recoil rate, but higher than metallic stents with −1.40 ± 3.83% recoil rate [21]. The foreshortening rate was 7.4% ± 2.0% (Fig. 2A), the radial compressing strength was 924.2 ± 76.2 mmHg (1.21 ± 0.100 atm) (Fig. 2C), lower than BVS (1.4 ± 0.2 atm) but higher than DESolve (1.1 ± 0.1 atm) [22]. Additionally, the number-average and weight-average molecular weight of PLS were 160845 ± 3665 g/mol and 84023 ± 3450 g/mol (Fig. 2B, Table S2), respectively. Overall, based on these comparisons with above PLLA based scaffolds, we consider the PLS applied in current research with fine mechanical properties. Based on previous studies, the time at which important events occur during the vascular repair process, post PLS implantation, are known with these being analyzed and discussed these events in detail in Fig. 1. Additionally, PLS showed good biocompatibility in main organs after implantation and degradation (Fig. S2).

3.2. Endothelial barrier function recovers faster at an early stage after PLS implantation

Reendothelialization is an important indicator of intimal repair and one of the major issues for clinical application of intravascular implants [1]. It was found that PLLA struts (~20%) were covered by the

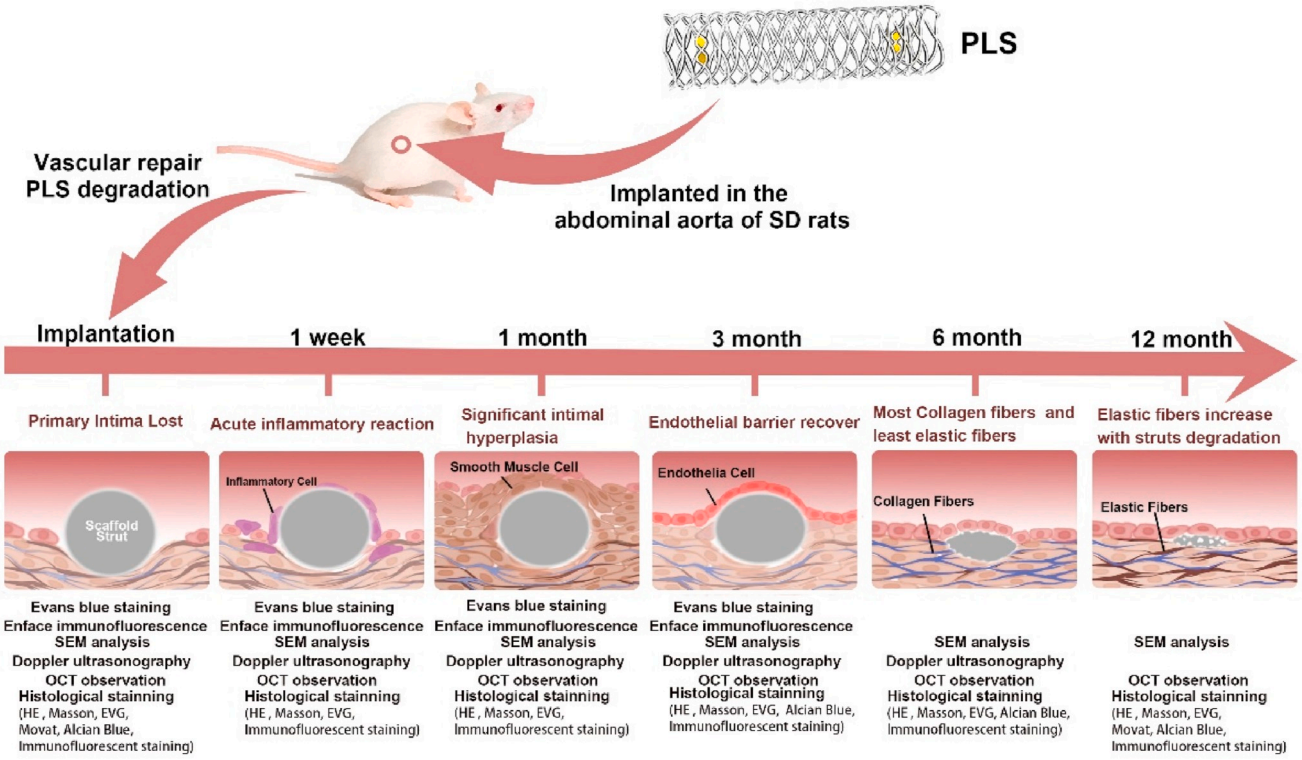

Fig. 1. Experiments applied at indicated time points after PLS implantation and important events at the corresponding time points.

neointima, 1-week post PLS implantation in the abdominal aorta of SD rats (Fig. 3A, B, C). Furthermore, neointimal coverage increased to ~80% and 100% at 1- and 3-months post-implantation (Fig. 3C). Moreover, it is noted that a thin layer of the neointima, at the interface of the neointima and the scaffold, was cracked after dehydration. Reendothelialization was completed after 3 months, although several structs remained fractured (Fig. 3A), possibly due to surface damage brought about by extrusion during implantation process.

By contrast, neointimal coverage was completed just 1 month after BMS implantation. After 1, 6 and 12 months, it was found that endothelial cells (ECs) were normally 'cobblestone-like' along the direction of blood flow, while the PLS implants first lost their original structure before degradation fully. In addition, the endothelium covering the proximal and distal segments was more orderly for PLS implants than that for BMS along with implantation (Fig. 3A), indicative of the gradual recovery of endothelial functions. We examined the expression of CD31, a typical endothelial marker, in the neointima of PLS implants (Fig. S3C) and found that there were virtually no $CD31^+$ cells on any struts at 1-week post-implantation, suggesting that neointimal formation had not yet started. CD31 expression near the struts was higher at 1-month post PLS implantation when compared to level at the other indicated time points (Fig. S3C) although its level remained elevated until 6 months. However, CD31 expression decreased to its lowest level at 12 months, indicating that there were phenotypic changes in the neointima over time considering different phenotypes of ECs. These results demonstrate that PLS implants can facilitate neointimal formation and reendothelializations.

An intact endothelial barrier safeguards the vascular intima from thrombosis, inflammation, and atherosclerosis. Different methodologies to evaluate the recovery of endothelial barrier function, including Evans blue staining, histological analysis, immuno-fluorescence staining, and SEM at the indicated time points. As the re-endothelization was completed within 3 months, while BMS showed faster neointima coverage at 1 month compared to PLS (shown in Fig. 3A, C2). At 1 week, the Evans blue-stained inner wall appeared and showed positive to negative staining of endothelium with time, indicating that endothelial barrier function had commenced after PLS implantation (Fig. 3E & S4). Combine with faster neointima coverage (Fig. 2A and 2C) in BMS at 1 month, we speculated that neointimal barrier function of endothelial cells in BMS were poor, for its more positive Evans blue and less VE-CAD staining (Fig. 3D), both of the staining could indicate the barrier function of endothelial cells. Subsequently, interactions between VE-CAD and β-catenin, the main proteins of endothelial cell adhesion and junctions, reflected the integrity of cell–cell contacts. Regarding endothelial coverage at 1-month post implantation, VE-CAD expression was much higher around the scaffold strut in the artery with an implanted PLS than that with an implanted BMS (Fig. 3D). Furthermore, we found that VE-CAD was mostly localized in the cytoplasm of ECs comprising arteries, whereas β-catenin was localized at the membrane after PLS implantation (Fig. S3B). An observation from xz and yz planes revealed that the expression of VE-CAD (red) and β-catenin (green) in the neointima was intact after PLS implantation, whereas the expression of only β-catenin (green) was noted after BMS implantation (Fig. S3A). We further examined the cell junction and thrombosis related proteins in neointima after PLS implantation (Fig. 3F, S5) and found discrete borders between adjacent ECs. The level of other cell junction proteins kept increasing post implantation, such as p120, which could stabilize VE-CAD, as well as zonula occludens-1 (ZO-1). As there was little neointimal formation at 1 week after implantation, we found that endothelial barrier function was not yet recovered. Furthermore, the levels of p120 and ZO-1 gradually increased (Fig. 3G), and peaked at 1 month post-implantation together with the re-arrangement of cells along the direction of blood flow. Levels of thrombomodulin (TM) were also examined, as the loss of TM function can cause spontaneous thrombosis in the arterial and venous circulation, with these levels found to have increased 3 months after PLS implantation. These findings indicate that PLS implantation can promote the recovery of endothelial barrier function when compared to BMS, which would probably ensure anti-inflammatory and anti-thrombotic effects of neointima, and we will present these effects and discuss at relevant contents.

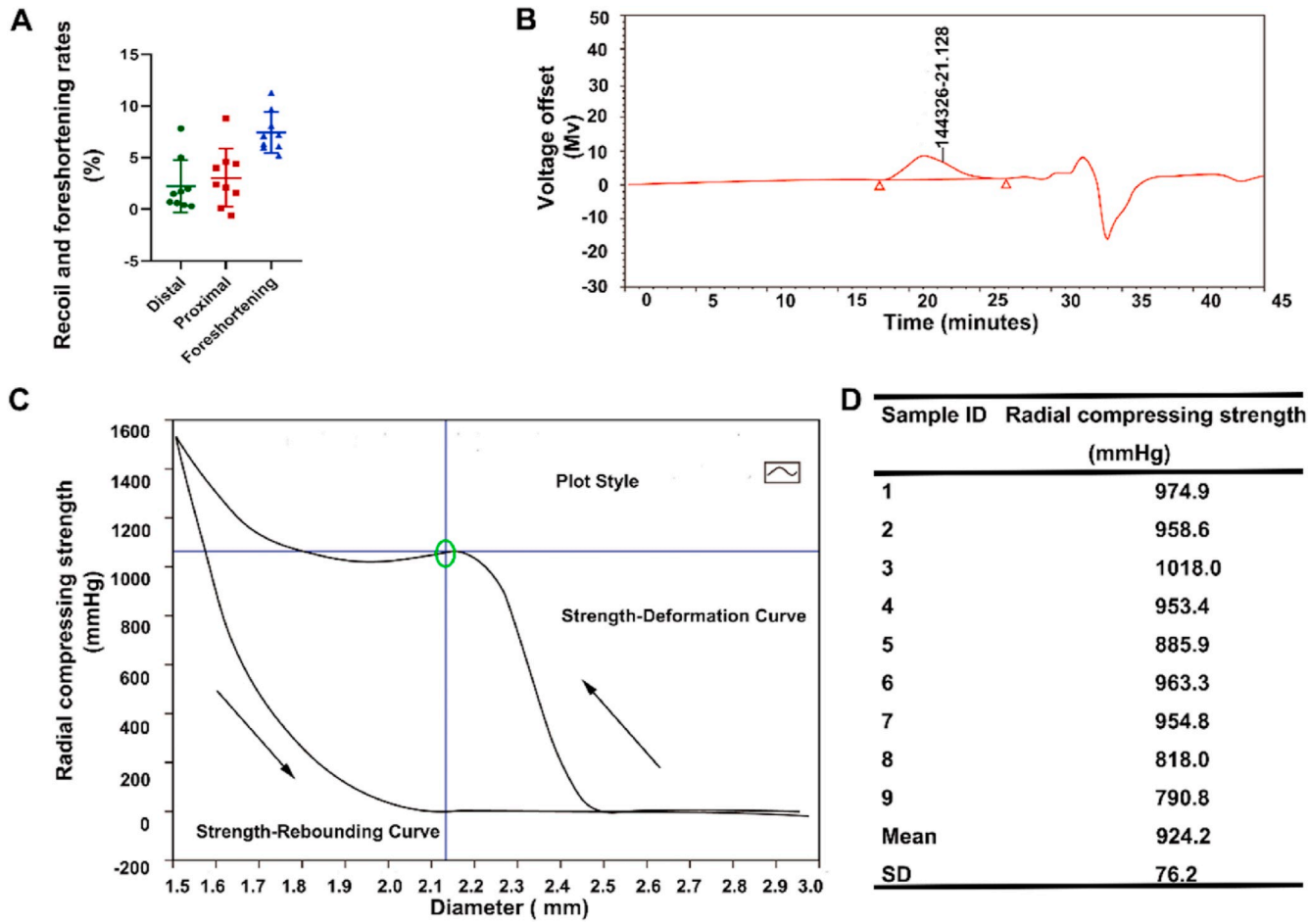

Fig. 2. Mechanical properties of PLS. (A) Recoil and foreshortening rate of PLS (n = 9). (B) Molecular weight test of PLS (n = 9). The two red triangles denote the start and end points of the integral area. It was found that '144326′ was the peak molecular weight (Mp) of the PLS and '21.128′ was the retention time of Mp. (C) Radial compression strength tests of PLS were carried out, with the upper-right showing the strength-deformation curve, and the bottom-left showing a strength-rebounding curve (black arrow showed the process of curve recorded). The center of the green oval is the maximum of radial strength. (D) Specific radial compressing strength tests data of PLS (n = 9).

3.3. Hyperplasia of the neointima after PLS implantation involves a two-process sinusoidal waveform-like transformative process

Hyperplasia of the neointima due to scaffold implantation is the main cause of late vascular restenosis and, until recently, has proved a challenging problem to solve [1]. Thus, the degree of intimal hyperplasia is an important index when evaluating successful vascular scaffold implantation. To examine this effect of implantation, the luminal areas of the abdominal aorta in proximal, distal, and middle segments at the implanted sites were evaluated by OCT at 12 months post (PLS or BMS) implantation. It was found that, on average, luminal area of the vessel segment was larger after implantation of PLS than that after implantation of BMS (Fig. 4A). After PLS implantation, the vascular luminal area (LA) and internal elastic laminal area (IELA) decreased significantly at 1, 3, 6, and 12 months when compared to that at week 1. From largest to smallest the areas of LA were ranked as 1 week, 1 month, 12 months, 6 months and 3 months while IELA was, similarly but not identically, ranked from largest to smallest as 1 week, 1 month, 6 months, 12 months and 3 months. Furthermore, the neointimal area (NIA) increased after 1, 3, and 6 months but not 12 months, with a largest to smallest rank of 1 month, 6 months, 3 months, 12 months, 1 week (Fig. 4E).

Significant hyperplasia of the neointima was observed 1-month post-implantation although this subsequently decreased, albeit moderately, after 3, 6, and 12 months (Fig. 4B). α-SMA expression in the neointima was low 1 week after PLS implantation, although this then increased between 1 and 3 months before decreasing from 6 to 12 months. No significant difference in α-SMA expression was observed between 1 week and 12 months (Fig. 4C). Conversely, this phenomenon was not observed after BMS implantation, with the results from 6 months post-implantation found in Fig. S6A. Furthermore, the expression of SM-MHC, a contractile SMC marker, was highest 1 week after PLS implantation, before steadily decreasing after 1, 3, 6, and 12 months. In addition, the expression of vimentin, a typical mesenchymal marker, was found to be highest after 3 months (Fig. 4D, G). When analyzed collectively, these data demonstrate that PLS implantation and PLLA degradation can both alter the phenotype of cells comprising blood vessels.

After BMS implantation, CD31 was only expressed by those cells closet to the lumen while α-SMA was mainly expressed in the neointima with little difference occurring temporally (Figs. S6B and C). This indicates that the cells in the neointima were mostly SMCs and also different when compared to those of the PLS group. The degree of stenosis was lowest at 1 week (~4%) after PLS implantation, markedly increased after 1, 3, and 6 months (~30%) before again decreasing after 12 months (~20%) (Fig. 4F). This data demonstrates the existence of a transformative phase for neointima hyperplasia and furthermore indicates that 6 months may be the key time point connecting the two distinct stages.

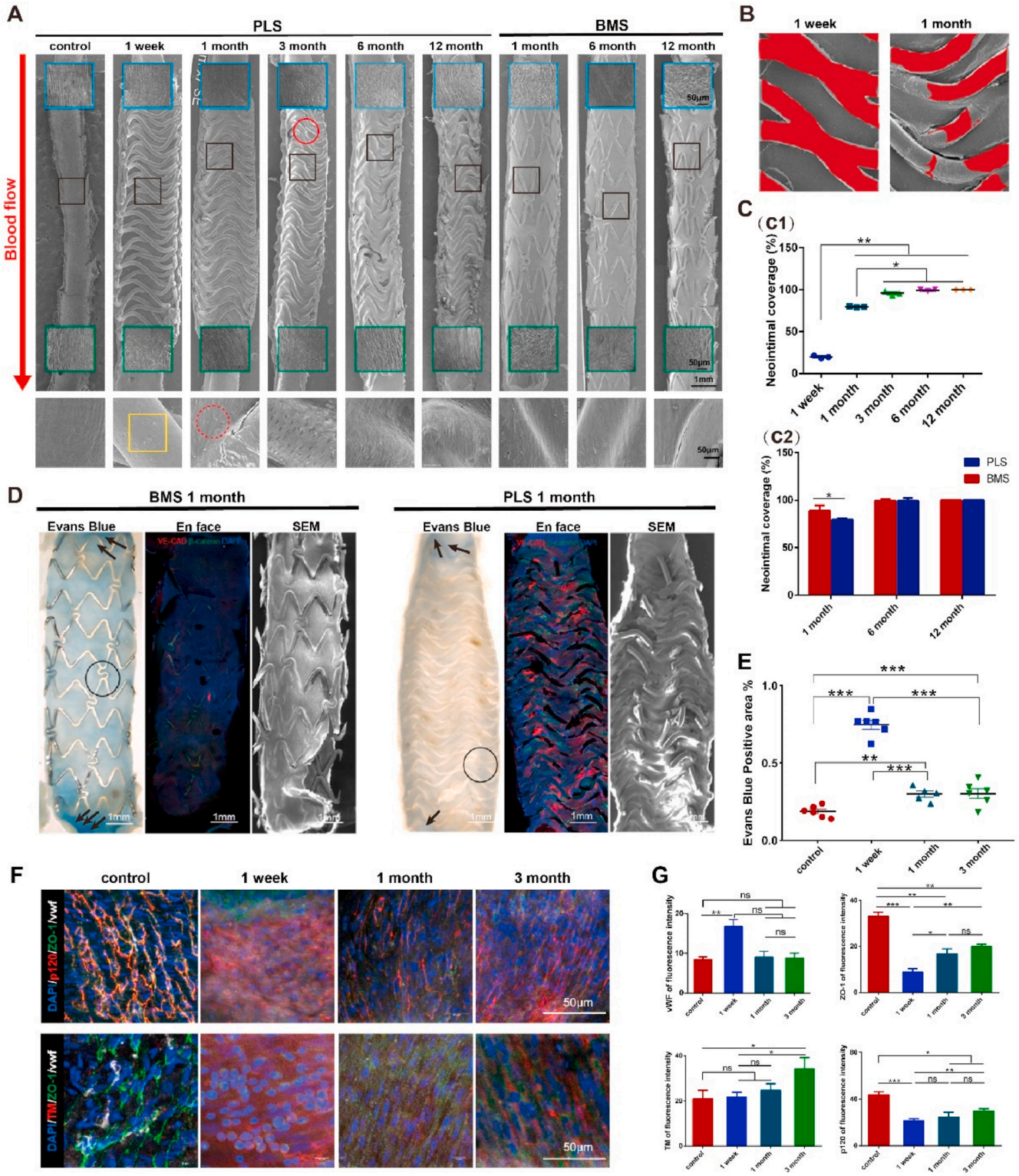

Fig. 3. Reendothelialization and recovery of endothelial barrier function in neointima after PLS implantation. (A) Reendothelializations after PLS and BMS implantation in abdominal aorta, shown in SEM images. Reendothelializations was completed after 3 months. The blue and green boxes indicate the proximal and distal segments near the scaffold and stent, respectively. The black boxes indicate the magnified images at each time point. The red solid-line circles indicate the cracked strut, whereas the red dashed-line circles indicate cobblestone-like ECs in neointima. The yellow boxes indicate the exposed strut without neointima. (B) Uncovered struts (red area) at 1 week and 1 month. (C) C1, Quantitative analysis of endothelial coverage after PLS implantation (n = 3); C2, Quantitative analysis and comparisons of endothelial coverage after PLS or BMS implantation at 1 month, 6 months and 12 months (n = 3). (D) and (E) Evans blue staining, distributions of VE-CAD and β-catenin and SEM after PLS and BMS implantation at 1 month (n ≥ 3), the black circle and arrow indicate deposit of Evans blue. (F) and (G), Immunofluorescence staining and quantitative analysis of fluorescence of cell junction and thrombosis related proteins in neointima (n ≥ 3). *$P < 0.05$, **$P < 0.01$, ***$P < 0.0001$.

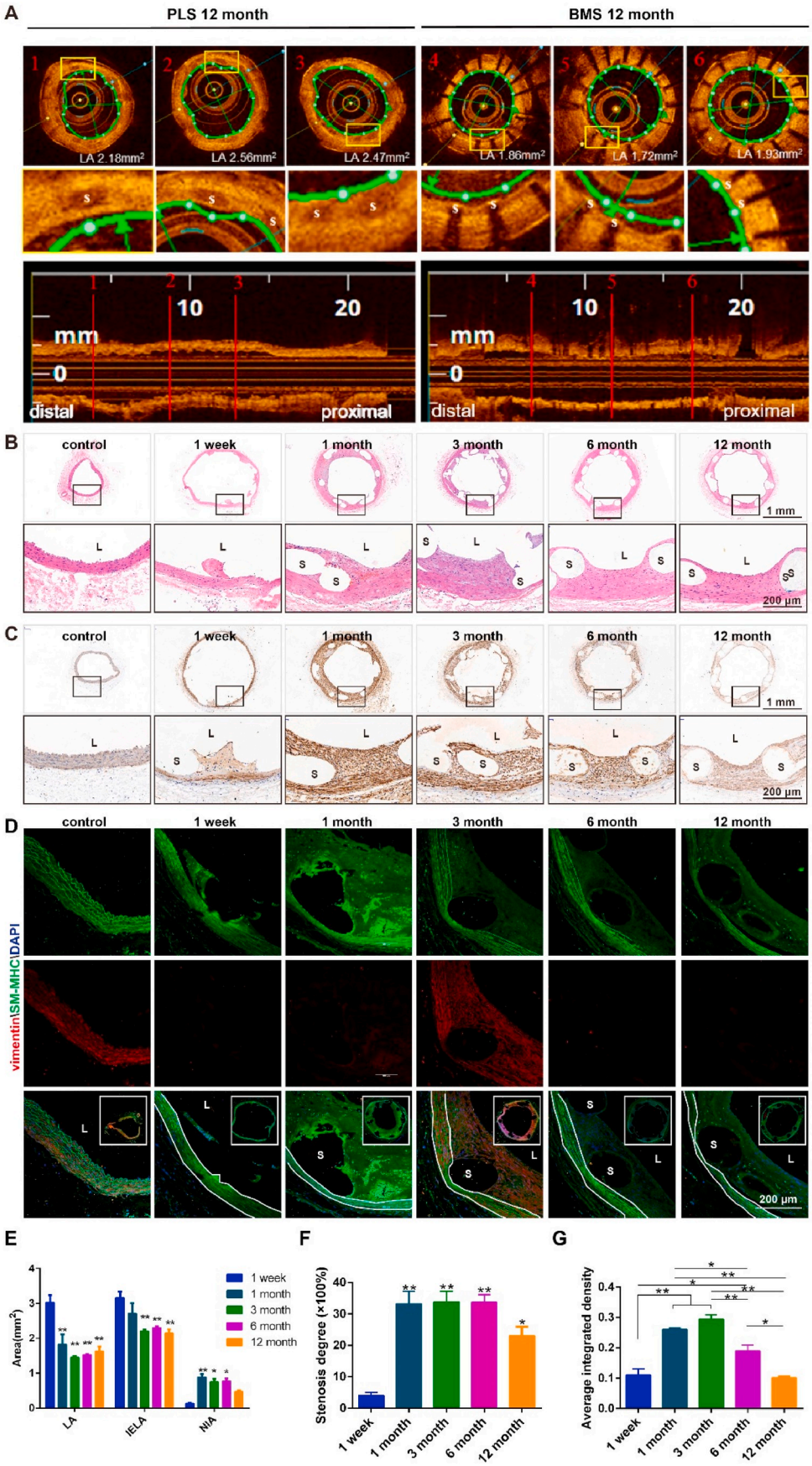

Fig. 4. Neointimal hyperplasia after PLS implantation in the abdominal aorta. (A) OCT images of different segments of the abdominal aorta at 12 months after PLS implantation, showing a larger luminal area than that after BMS implantation. (B) Images of the scaffold segments of the abdominal aorta stained with HE after implantation. (C) α-SMA immuno-histochemical staining of the vascular segment after scaffold implantation in the abdominal aorta. (D) Vimentin (red) and SM-MHC (green) immuno-fluorescence staining of the vascular segment after PLS implantation. (E) Area of the vascular segment after scaffold implantation (n = 3). LA, luminal area; IELA, internal elastic laminal area; and NIA, neointima area. (F) Stenosis degree of the vascular segment after scaffold implantation (n = 3). (G) Quantitative analysis of vimentin expression in the neointima using the immunohistochemistry results. L, lumen and S, scaffold/stent strut (n ≥ 3). *$P < 0.05$, **$P < 0.01$.

3.4. Hemoperfusion is enhanced accompanying PLS degradation

The main purpose of scaffold implantation is to restore the blood flow in vessels [1]. To test this, the vascular patency in abdominal aortas of SD rats was examined by Doppler ultrasonography at the same temporal steps indicated previously, after 1 week and 1-, 3-, and 6-months post implantation. We observed that the reticular structure of the scaffold within the vascular wall was clearly visible 1-week post-implantation but subsequently undetectable after 1, 3, and 6 months in PLS, while kept visible at 1 month after implantation of BMS (Fig. 5A). The velocity of blood flow at the scaffold segment was measured at 239.4 ± 43.97 mm/s 1-week post PLS implantation before markedly increasing to 575.6 ± 43.48 mm/s, 612.4 ± 64.05 mm/s, and 675.9 ± 71.25 mm/s at 1, 3, and 6 months, respectively (Fig. 5B). Additionally, the vascular diameter was measured by OCT at different temporal points post PLS implantation. A fault was discovered between the scaffold segment and the proximal or distal segment after 1 week (Fig. 5D). The serrated edge of the implanted vessel was smooth at 3 months indicated by positions pointed by white arrows with less jagged edges while the scaffold struts were entirely covered by the neointima after 12 months, a strong indicator of neointimal formation. The vascular diameter curve, measured at the site of PLS implantation, showed that the lumen diameter, which was initially 1.2 ± 0.125 mm, increased to 2.004 ± 0.065 mm 1-week post-implantation before decreasing to 1.5 ± 0.040 mm, 1.5 ± 0.041 mm and 1.446 ± 0.035 mm after 1, 3 and 6 months respectively (Fig. 5C). This then increased again slightly, although not to week 1 levels, to 1.628 ± 0.074 mm after the full 12 months. There were no obvious differences among 1, 3, 6, and 12

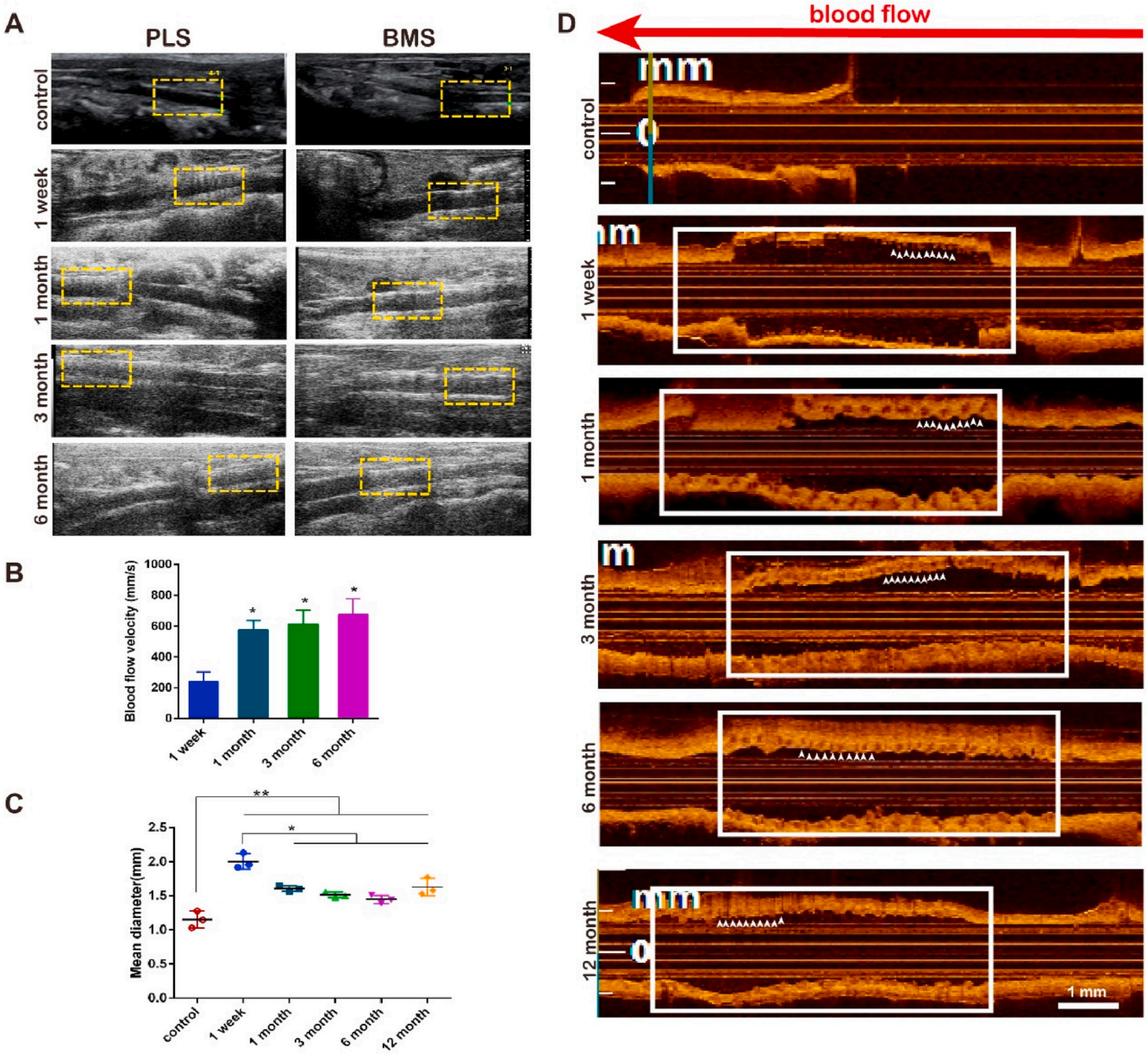

Fig. 5. Vascular hemoperfusion after PLS implantation. (A) Results of Doppler vascular ultrasonography at 1 week and 1, 3, and 6 months after PLS or BMS implantation reveal the continuous lumen patency. The yellow dotted-line boxes indicate the location of the scaffolds. (B) Blood flow velocity of the scaffold segment as measured by Doppler vascular ultrasonography shows the increased blood flow velocity (n = 3). (C) Mean diameters of the implanted segment at 1 week, 1 month, 3, 6 and 12 months after implantation show that the diameter of the vessel decreased and then increased. (D) OCT images at 1 week, and 1, 3, 6, 12 months after PLS implantation reveal the late-stage lumen patency. The positions pointed by white arrows with more or less jagged edges indicate the smoothness of implanted segment. The white line boxes indicate the location of the scaffolds (n = 3). *$P < 0.05$, **$P < 0.01$.

months, these diameters higher than control (**$P < 0.01$), lower than 1-week (*$P < 0.05$) (Fig. 5C). Furthermore, OCT images of stented arteries at different temporal points demonstrated the overexpansion of vessel diameter at 1-week post implantation when compared to all later time points, but no obvious differences between these later temporal points of 1 month–12 months. These measurements indicate no obvious lumen hyperplasia or lumen loss particularly at late stages, especially at 12-month (Fig. 4E, F, 5C, 5D). These findings indicate that the size of the vascular lumen was decreased, suggest advantages of PLS application at late stage.

3.5. Significant PLS degradation occurs from 6 months and differential ECM responses at distal and proximal segments at 12 months

Previous studies have investigated PLLA degradation *in vitro* although less is known about this *in vivo* [23–25]. We examined molecular weight (Mw) and number-average molecular weight (Mn) of PLS at different time points *in vitro* last for one year, they exhibited same degradation trend (Fig. S7) with minimum Mw and Mn at one year, revealed continuous degradation. We also examined both the exterior and interior of PLLA struts at different temporal points. Cross-sections of PLLA struts revealed a smooth surface with a dense framework before implantation which immediately expanded post implantation (Fig. 6A). Minimal structural changes were observed at 1-week and 1-month post-implantation. Block stratification occurred at 6 months, while the structure then became looser, due to the increased porosity after 12 months, indicative of degradation of the scaffold (Fig. 6A). Similarly, the surface of the scaffold was observed to be fully intact 1-month post-implantation, before pores started to develop after 6 months and become clearly visible at 12 months (Fig. 6B). To further analyze degradation of the scaffold, the degraded fragments of the struts were subsequently examined. The outline of the scaffold was found to be smaller and more blurred at 12 months when compared with that which was observed by OCT images after 6 months with the clearest outline of the strut seen at 3 months (Fig. 6E, H). Additionally, the fragments which had been stained blue were observed near the scaffold at 6 and 12 months, but not at 3 months (Fig. 6F, I), which is indicative of scaffold degradation. Furthermore, the results of Alcian blue staining indicated partial degradation of PLLA struts after 12 months (Fig. 6G, J). Interestingly, we observed a stronger remodeling in proximal compared to distal segments of PLS at 12 months post-implantation by stronger black color indicated elastin fibers while α-SMA was the other way around, and there were no significant differences in scaffold degradation (Fig. 6C). Additionally, the expression and distribution of CD31 was much stronger in proximal compared to distal segments of PLS at 12 months post-implantation (Fig. 6D). We speculated which might have been due to independently formation of elastin by ECs. Although this initial study has shed some light on this process, further studies are needed to confirm these findings.

Throughout this study it was found the degradation of PLS was generally accompanied with inflammatory responses. More specifically, we observed a large infiltration of inflammatory cells, and more specifically that the levels of inflammatory markers CD68 and CD11b were increased. These were both primarily distributed around the scaffold struts from 1-week to 1-month post PLS implantation, before continually decreasing up to12 months (Fig. 7A, B, C).

To examine the inflammatory effects of PLLA on SMCs, macrophages with various phenotypes (M0, M1, and M2) were induced by THP-1 and co-cultured with SMCs in the presence of PLLA. When compared with M0 and M2 macrophages, it was found that M1 macrophages promoted the proliferation of SMCs regardless of the PLLA treatment, whereas PLLA significantly enhanced the proliferation of SMCs regardless of the macrophage phenotype (Fig. 7D). These findings demonstrate that the inflammatory response induced within the first 6 months by PLS implantation can promote the proliferation of SMCs and moreover induce hyperplasia of the neointima.

Subsequently, co-staining of CD68 and CD206 (Fig. 7G) or CD68 and CD197 (Fig. 7H) presented more co-localization at 1 month and 3 months, while less co-localization were discovered after 3 months, compared to other temporal times, indicating both M1 and M2 macrophage were involved in inflammation responses, which was also in line with *in vitro* experiments of M1 and M2 post PLS implantation. Further, quantitative analysis revealed that M2 contributed more in inflammation process (Fig. 7E, H), especially at late times. We however noted that the inflammatory response elicited by PLS was different to that from BMS (Figs. S8A and B and our previous studies [26]). The results obtained reveal that the inflammatory response in the neointima of vessels is strongest in the early stage after PLS implantation before gradually attenuating up to 6 months. These findings lead us to speculate that the accumulation of cellular components, as well as the release of inflammatory factors into the blood, may be stimulated by the interventional process and changes within the hemodynamic environment, thereby leading to inflammation at an early stage as well as its subsequent gradual decrease in time [27].

3.6. ECM response is conspicuous from 6 months after significant degradation of PLS

BRS can temporarily support blood vessels to allow sufficient hemoperfusion [1]. Moreover, as they are gradually absorbed by blood vessels after implantation this can eliminate the likelihood of any harmful long-term reactions to the foreign body. Furthermore, PLS biodegradation may positively influence, and even restore, the plasticity and remodeling of arterial vessels through altering the compositions of ECM. We examined ECM components through Masson's trichrome, Verhoeff Van Gieson (EVG), and Sirius red staining. It was found that the percentage of collagen fibers in the neointima markedly increased from ~20% at 1 week to ~60% at 1, 3, 6, and 12 months after PLS implantation (Fig. 8A, D), whereas the percentage in the media almost doubled from ~50% at 1 week to ~90% at 6 months before decreasing to ~60% after 12 months (Fig. 8A, E). Changes in the different types of collagens, after PLS implantation, were further analyzed by applying Sirius red staining (Fig. 8C). It was found that the percentage of type I collagen fibers, which were stained red or yellow, decreased steadily up until 6 months but subsequently recovered between 6 and 12 months. Additionally, the arrangement of type I collagen fibers improved when examined 12 months post-implantation as compared to earlier temporal points. However, the percentages of type III and other types of collagen fibers continually increased over time. During vascular repair, the quantity, structure, and composition of collagen fibers were altered. Additionally, the percentage of elastic fibers decreased markedly from ~25% at 1 week to 3% at 6 months before recovering to the original week 1 level of 25% after12 months (Fig. 8B, F). This data shows that while collagen fibers increased, elastic fibers decreased in vessels up to 6 months after PLS implantation, followed by the establishment of normal vessels at 12 months. It seems that 6 months was a key turning point.

3.7. Decreased mechano-growth factor expression associates with reduced mechanical support induced by PLS degradation

PLS degradation generally leads to mechanical changes in scaffolds, which can be detected by surrounding vascular cells, like ECs and SMCs thereby bringing about changes in mechano-sensitive proteins. However, due to the complex degradation of PLS, application of computational fluid dynamics (CFD) to demonstrate the mechanical changes of PLS remains difficult to achieve. It is therefore necessary to apply mechanical sensor proteins to show these changes, such as mechano-growth factor (MGF) and bone morphogenetic protein 2 (BMP2). Besides, blood vessels can respond to mechanical environments, which promoted us to apply both MGF and BMP2 as an indicator of mechanical changes. The levels of MGF and BMP2 were both found to be high in the neointima at 1 month after PLS implantation (Fig. 9D and E), while the

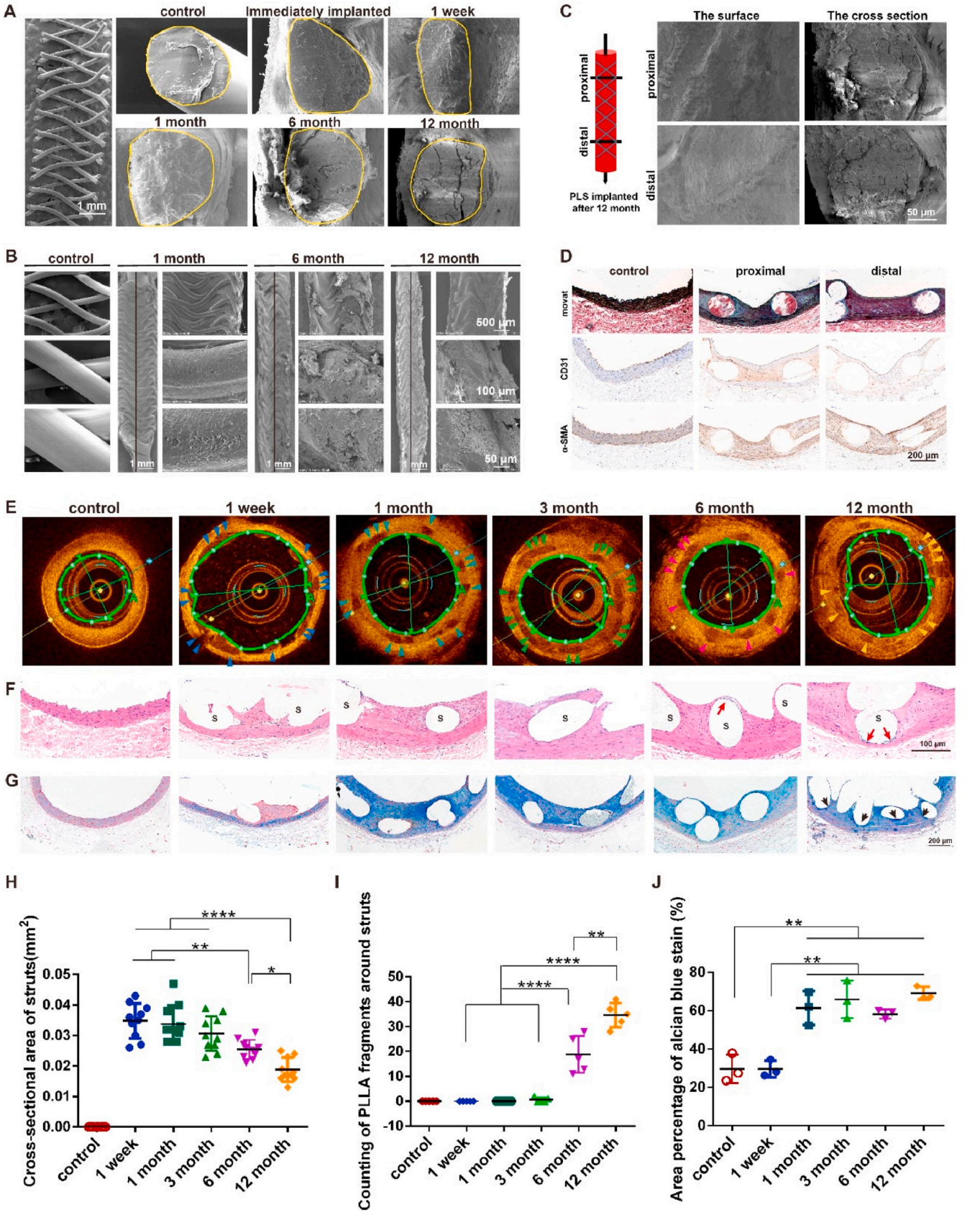

(caption on next page)

Fig. 6. *In vivo* degradation of PLS after implantation. (A) *In vivo* degradation of PLS after implantation by SEM. The yellow solid lines indicate cross-sections of the scaffold strut. (B) Surface degradation of PLS after implantation. The black line as the boundary of the intima that was scraped off. (C) SEM images of proximal and distal segments of the vascular endothelium at 12 months after PLS implantation. (D) Movat staining, CD31 and α-SMA immunohistochemistry of proximal and distal segments of the vascular endothelium at 12 months after PLS implantation. (E) OCT images of the degraded scaffold strut after PLS implantation, the scaffold strut is indicated by red (3 months), white (6 month) and blue (12 months) arrows. (F) HE staining of the degraded scaffold strut after PLS implantation. The red arrows indicate debris of PLS degradation. S, scaffold. (G) Alcian blue staining after PLS implantation. The black arrow indicates the completely degraded PLS. (H) Statistical analysis of the area of PLS struts at 3, 6, and 12 months from OCT results ($n \geq 3$). (I) Statistical analysis of the PLLA fragments around PLS struts at 3, 6, and 12 months from HE stains ($n \geq 3$). (J) Statistical analysis of the area percentage of Alcian blue staining at 3, 6, and 12 months ($n = 3$). $^{*}P < 0.05$, $^{**}P < 0.01$, $^{***}P < 0.0001$.

levels of both of these subsequently decreased after 3, 6, and 12 months while a reduction in hyperplasia of the neointima (Fig. 9D and E) was also found. MGF was predominantly expressed in the media at 3 months post-implantation, whereas BMP2 was mainly concentrated near the scaffolds of the media and neointima (Fig. 9A). The levels of both proteins increased in the short-term post PLS implantation before decreasing after 6 months (Fig. 9D and E). To further investigate the effects of different mechanical changes on the expression of MGF in vascular cells, HUVECs were treated with shear stress at 6 and 12 dyne/cm^2 for a period of 6 h. This revealed that MGF expression levels increased proportionally with shear stress while the concentration was highest in the nuclei of treated cells when compared with untreated cells (Fig. 9B and C). Additionally, SMCs were treated with 10% of 1 Hz cyclic stretch for a period of 12 h with this test also showing that MGF levels increased significantly in treated cells when compared to untreated cells (Fig. 9F and G). These findings demonstrate that PLS degradation brought about mechanical changes as well as affecting the proliferation and migration of vascular cells through MGF.

4. Discussion

As a novel device for cardiovascular interventions, BRS can provide temporary support for blood vessels, prevent acute vascular recoil post implantation and furthermore reduce the incidence of restenosis [1,28]. After implantation these scaffolds will gradually degraded and due to absorption by the surrounding vascular tissue, their localized mechanical effects disappear over time [18,26,28]. This complex degradative process may induce different vascular responses, which can alter both the phenotype and functions of vascular cells when compared with traditional, metal drug-eluting stents. It is therefore necessary to investigate this degradation process, with a specific focus on the effects of BRS degradation on the phenotypic transformation and changes in the deposition of ECM components. Such studies may lead to new insights on how to effectively minimize scaffold restenosis, thrombosis and local inflammation in future clinical applications. Through use of an *in vivo* rat model, this study focused on vascular repair and explored the temporal course changes and correlations of vessel remodeling–scaffold degradation which may help to improve the design of next-generation BRS and enhance vascular recovery. Various parameters were examined pre and post PLS implantation while mechanical tests of PLS, endothelial function, vascular remodeling, and the relationship between scaffold degradation and vascular cell phenotypic changes were examined. Our findings indicate that the implantation with predominant mechanical support of PLS and *in vivo* degradation of BRS resulted in a "two-process" vascular repair, with the transition from the first to the second stage occurring at 6 months. Further studies of this "two-process" transformative may result in new strategies for designing drug coating and clinical combination drug therapy.

Traditional BMS are manufactured through laser carving. Patients are required to take anticoagulants for a long period of time post implantation, and may also suffer from ineluctable stent restenosis and fatigue fracture. BRS is expected to eliminate such adverse effects, and PLLA is recognized as a material with good biocompatibility which provides mechanical support. At present, most BRS on the market are processed by a laser engraving method where the cross-sectional area of the support rod is rectangular. In this study, we designed and printed a 3-D PLS, with good recoiling rate. This also demonstrated greater radial strength when compared with Xinsorb [21,22]. Additionally, it is clear that a higher foreshortening rate could initiate more significant vascular restenosis injuries. The foreshortening rate of PLS was 7.4% ± 2%, higher than 6.89% of vascular scaffold Version 1.1 (BVS 1.1, Abbott Laboratories) [30] and higher than that of stainless steel stents [29]. However, it is common that the foreshortening rate of PLLA, or polymer based vascular scaffolds, was much higher than stainless steel stents (due to an increased strut diameter) during deployment. For example, in a strut geometry study the author reported that foreshortening rate of PLLA scaffolds ranged from 2.3% to 13.9% [31]. In another finite element investigation of graphene oxides reinforced PLLA scaffold, the foreshortening rate reached 21% [32]. Based on these comparisons, we speculate that PLS possesses suitable mechanical properties. Additionally, PLS was designed with circular cross-section, as a circularly shaped strut can reduce the disturbance of blood flow and is more beneficial to the normal function of endothelium when compared to the rectangular strut [33]. With the same strut thickness, the circular strut has a smaller cross-sectional area and possesses different patterns of degradation and vascular reaction *in vivo*. This may be reflected by intimal repair and vascular remodeling which were both discussed in depth in the preceding section.

The vascular endothelium creates a barrier between the vessel wall and lumen, and rapid reendothelialization post scaffold implantation can effectively block any contact between the scaffold and blood, thereby reducing the likelihood of inflammation and thrombosis [23]. Additionally, the endothelial dysfunction can stimulate atherosclerosis [34]. Thus, the early recovery of endothelial function (within 6 months of scaffold implantation) is crucial in preventing restenosis and late thrombosis [35,36]. In addition to the reendothelialization kinetics and neointimal thickness, the integrity and permeability of the vascular endothelium further reflect the recovery status of neointimal function. Previous studies have reported that the inflammatory and anti-proliferative effects of DES can delay reendothelialization [37]. We found that reendothelialization was complete 1 month after the implantation of either PLS or BMS. The morphology of the neointima gradually transformed into normal vessels over time post PLS implantation although this was not the case of the neointima after BMS implantation [38,39]. In addition, ECs can prevent the entry of white blood cells and lipoproteins into the inner subcutaneous space through the expression of adhesion proteins [40], such as VE-CAD, which is stabilized by β-catenin and p-120, and then indirectly anchored to the F-actin cytoskeleton [41]. VE-CAD has previously been reported to mediate the integrity of the endothelial cell barrier through Ca^{2+}-dependent interactions [38]. We therefore examined the barrier function of the neointima after PLS implantation from various aspects, including the expression level of VE-CAD, β-catenin, p120, ZO-1, and TM. It was found that PLS implantation increased the levels of these proteins concurrently with the degradation of PLS, as well as maintaining the integrity of the endothelial cell barrier and preventing thrombosis. These findings indicate that PLS implantation facilitates recovery of the neointima. We therefore conclude that, in addition to in-stent restenosis (ISR) and reendothelialization, the barrier function of the vascular endothelium should be considered as a new reference parameter when evaluating the performance of PLS.

In ideal circumstances, after implantation, PLLA based BRS will

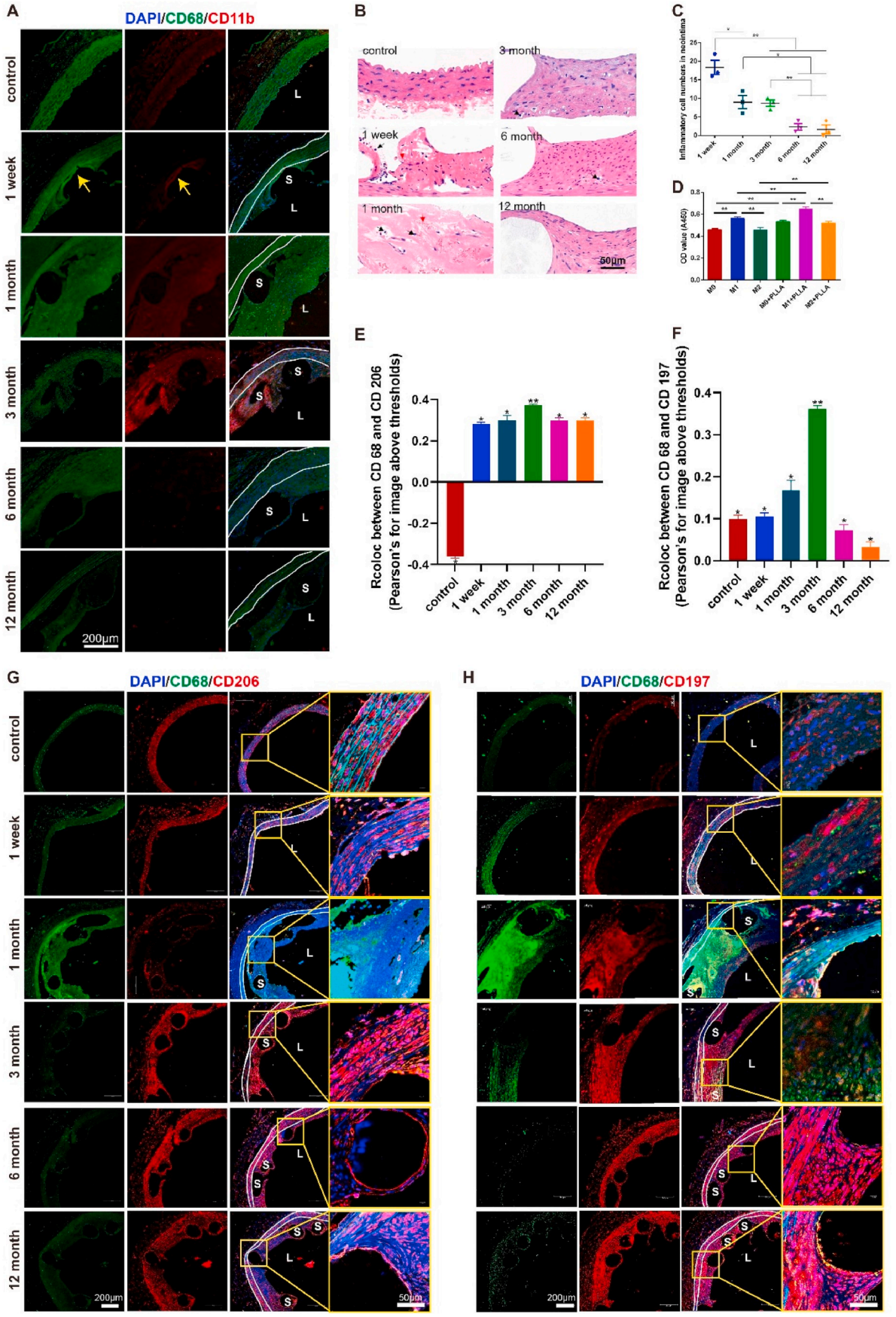

(caption on next page)

Fig. 7. Inflammatory responses induced by implantation and degradation of PLS *in vivo* and *in vitro*. (A) CD68 (green) and CD11b (red) immuno-fluorescence staining of the vascular segment after PLS implantation indicates that the inflammatory response increased and then decreased over time. The area between the white solid lines represents the media. (B) Analysis of the inflammatory reaction in the neointima by HE staining after PLS implantation shows inflammatory cell infiltration at 1 week and 1 month. The red arrows indicate red blood cells, whereas the black arrows indicate inflammatory cells. (C) Inflammatory cell numbers in the neointima after PLS implantation gradually decreased over time (n = 3). (D) PLLA promotes the proliferation of macrophage-induced SMCs (n = 3). (E) Co-localization analysis of CD68 and CD206 by Pearson's rate before and after implantation of PLS presented increasing to 3 months then decreasing (n = 5). (F) Co-localization analysis of CD68 and CD197 by Pearson's rate before and after implantation of PLS also presented increasing to 3 months then decreasing (n = 4). (G) CD68 (green) and CD206 (red) immuno-fluorescence staining of the vascular segment after PLS implantation indicates that the M2 macrophage expression kept increasing to 3 months then decreasing post implantation. The yellow box indicated enlarged position. (H) CD68 (green) and CD197 (red) immuno-fluorescence staining of the vascular segment after PLS implantation indicates that the M1 macrophage expression also kept increasing to 3 months then decreasing post implantation. The yellow box indicated enlarged position. *$P < 0.05$, **$P < 0.01$, S, scaffold/stent and L, lumen.

degrade over a period of roughly 2–3 years before eventually disappearing. However, the *in vivo* degradation time has been found to be much longer than initially expected. Thus, as it may be present for longer than previously expected, it is important to explore the adverse effects of PLS degradation after implantation, such as late thrombosis, secondary atherosclerosis, and vascular calcification [42]. PLS degradation occurs in two phases: surface degradation, where the permeation of water, the loss of mass from the exterior to the interior as well as the surface area can affect the degradation rate; and volume degradation, wherein the hydrolysis rate, mass loss of the polymer balance, and the rate of degradation are major factors [43]. Our findings indicate that both external and internal degradation of the scaffold occurred post implantation. Despite the structure and supporting force of the PLS being maintained during the first few months, scaffold degradation became pronounced and the structure started to change at 6 months after implantation. After this same amount of time, the scaffold struts became blurred which coincided with the discontinuity of the structure and loss of its mechanical properties [44]. An interesting finding was that the degradation of PLLA after implantation was significantly different from Zn or Fe based biodegradable endovascular alloy stents, for corrosion rate of alloy could be related to the amount of eutectic constituent found in the microstructure of their alloy [11,12], while PLS showed non-uniform with faster degradation in the distal compared with the proximal end, leading to different degrees of vascular repair and reconstruction of ECM. In addition, the debris from PLLA degradation which maintained in the tissue for uncertain repair period draws our attention, as our latest research proved the engulfment of ECs may promote their proliferation and angiogenesis, inflammatory response, and fibrosis [45], whether and how these PLLA debris would be engulfed by endothelial cells in neointima and influence the vascular repair is worthy of further study. Whether lactic acid produced by PLLA degradation causes cell phenotypic transformation also deserves further study. Besides, degradation in animals is different from humans, and current degradation tests of materials mainly depend on weight loss, which is lack of accuracy. We proposed that more clinical data about PLLA and corresponding OCT data at indicated time are needed to reconstruct, provide quantitative evaluation of *in vivo* PLLA degradation.

Vascular inflammation is a major cause of ISR and stent thrombosis which might be observed throughout the degradation of PLS *in vivo*. The inflammatory response after scaffold implantation is first manifested by the infiltration and accumulation of inflammatory cells around the scaffold strut [46]. PLLA itself can also induce inflammatory responses in blood vessels [47]. Neutrophils and monocytes are involved in early and acute inflammation, whereas macrophages are involved in late and chronic inflammation [48], and these immune cells can be reliably marked with CD68 and CD11b [24,49]. We found that the early expression of CD68 and CD11b around the scaffold was significantly stronger after implantation than that before implantation, indicating that neutrophils and monocytes are mainly involved in the early "stage". The vascular inflammatory response was gradually reduced in the last 6 months after scaffold implantation, which might have been due to the restoration of endothelial function and the fact that TM protects ECs and the vasculature by depressing inflammatory injuries [50]. Furthermore, SMCs can produce a strong pro-inflammatory response, whereas the ECM can generate a significant anti-inflammatory effect. The balance between the pro-inflammatory and anti-inflammatory effects of SMCs has been reported to determine the pathology of the media [51]. A previous study has reported that SMCs in atherosclerotic plaques express macrophage markers, and these macrophage-like SMCs can phagocytose lipids [52]. Our findings revealed that PLLA could promote the proliferation of SMCs in the presence of M1 macrophages that secrete pro-inflammatory cytokines and chemokines. The inflammatory response after PLS implantation is influenced and mediated by multiple factors, and gradually match the repair process of blood vessels.

Vascular intimal hyperplasia and remodeling occur throughout PLS implantation, during which time the ECM and SMCs interact to play important roles in the recovery of vessel morphology and function. Vascular remodeling is responsive to the biomechanical environment and determined by the type, composition, and distribution of the ECM, which is closely related to the number and phenotype of SMCs. The presence of a sufficient percentage and a specific phenotype of SMCs is necessary not only for the production of the matrix but also for the structural adaptation of SMCs, which influence the biochemical composition of the ECM and affect the remodeling of blood vessels. We found that the expression of α-SMA and the percentage of collagen fibers increased after PLS implantation and then decreased over time, whereas the percentage of elastic fibers decreased and then increased at 6 months post-implantation. Thus, SMCs can affect vascular remodeling, and their phenotypic changes are particularly important for vascular repair after scaffold implantation.

During vascular remodeling, vessels can respond to the degradation of scaffold, accompanied by the changes of related factors for mechanical regulation. MGF is an isomer of insulin-like growth factor 1 (IGF-1) that can respond to pressure, injury, and disease [53,54]. BMP family members play important roles in bone repair by rapidly up-regulating the levels of endogenous BMP2 and phosphorylated Smad, and these proteins are responsive to mechanical signals [55]. In addition, MGF can promote BMP2 expression, as was shown in a previous study of bone repair [56]. MGF expression was mainly found in the media and adventitia of control vessels, whereas BMP2 was predominantly expressed in the media (Fig. 8A). BMP2 expression was significantly increased in both media and adventitia at 1 week after PLS implantation, whereas MGF expression was increased in the media. We found that MGF and BMP2 could respond to scaffold degradation at the same time, and their levels increased and then decreased along with scaffold degradation, which was consistent with the process of vascular repair.

Based on our previous discussion, we proposed that vascular repair after PLS implantation can be divided into two different but connected processes (Fig. 10): "0–6 months" (during which time there is vessel inflammation, neointima hyperplasia, and endothelial re-functionalization), which is characterized by new stimulations due to scaffold implantation, and "after 6 months" (during which time there is vessel recovery, scaffold degradation, and vascular remodeling), which is characterized by the formation of normal vessels. There is no clear boundary between these two processes, which led us to speculate that the transition may have taken place between 6 and 12 months. The recovery of endothelial barrier function and vascular remodeling after the two processes can effectively reduce restenosis and the incidence of

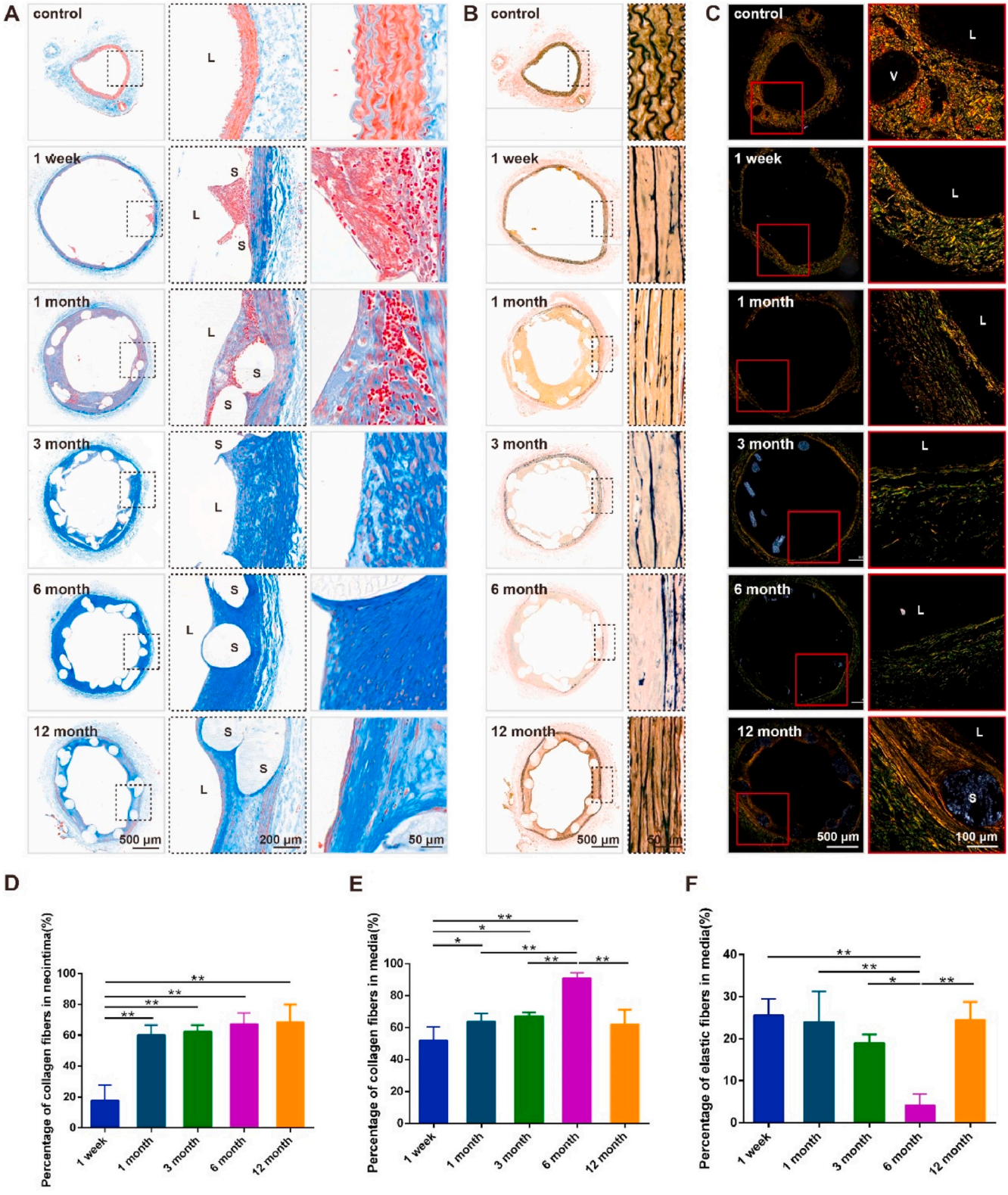

Fig. 8. Vascular ECM responses of abdominal aorta after PLS implantation. (A) Masson staining of the vascular segment at 1 week and 1, 3, 6, and 12 months after scaffold implantation in the abdominal aorta. (B) EVG staining of the vascular segment at 1 week and 1, 3, 6, and 12 months after scaffold implantation in the abdominal aorta. (C) Sirius red staining of the vascular segment at 1 week and 1, 3, and 6 months after scaffold implantation in the abdominal aorta. (D) Percentage of collagen fibers in the neointima of the vascular segment after scaffold implantation in the abdominal aorta (n = 3). (E) Percentage of collagen fibers in the media of the vascular segment after scaffold implantation in the abdominal aorta (n = 3). (F) Percentage of elastic fibers in the media of the vascular segment after scaffold implantation in the abdominal aorta (n = 3). *$P < 0.05$, **$P < 0.01$.

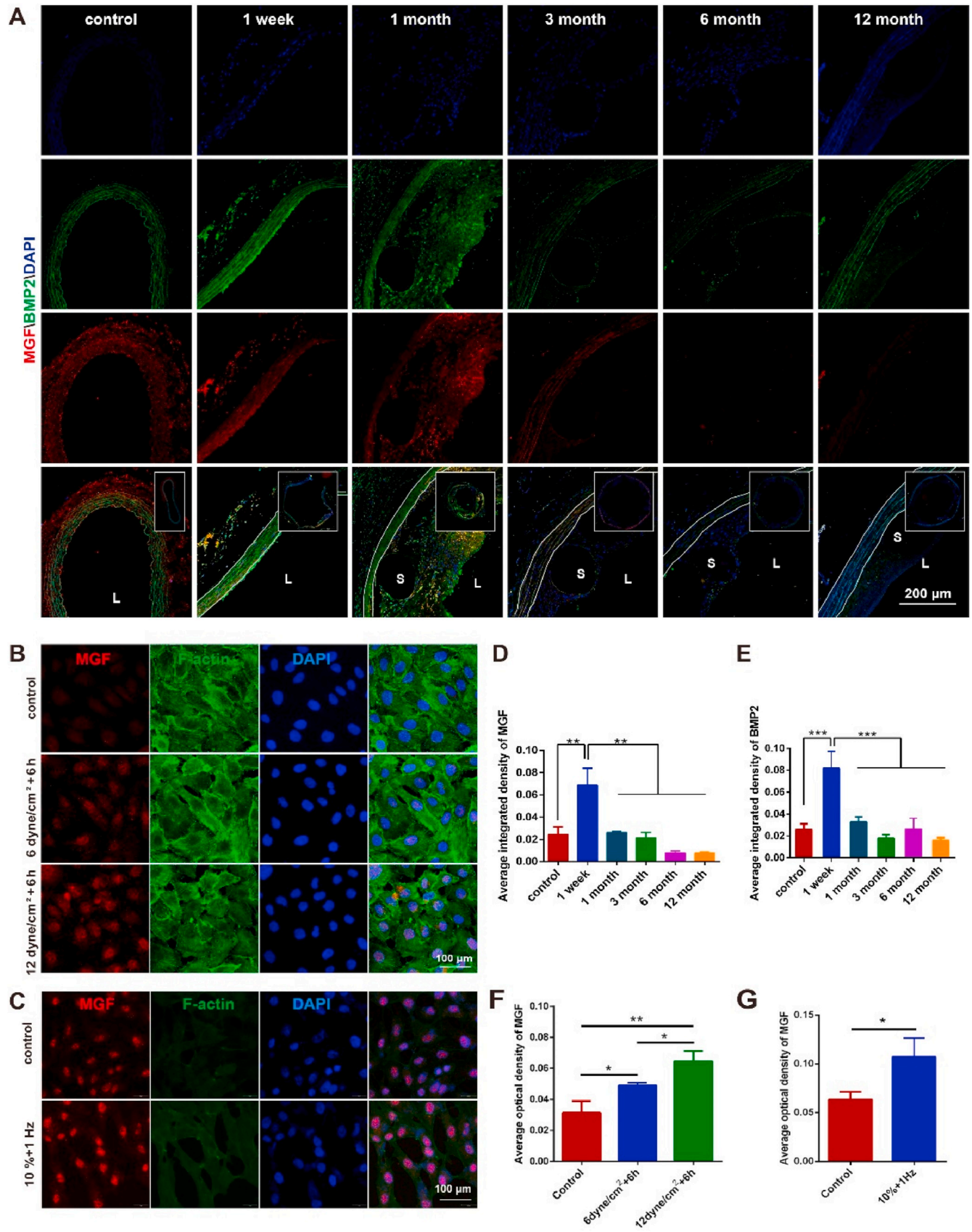

Fig. 9. Vascular mechanical response to the degradation of PLS. (A) MGF (red) and BMP2 (green) immuno-fluorescence staining after PLS implantation in the abdominal aorta. (B) MGF immuno-fluorescence staining of HUVECs after shear stress loading for 6 h. (C) MGF immuno-fluorescence staining of SMCs after cyclic strain for 12 h. (D) Average optical density of MGF after PLS implantation ($n \geq 3$). (E) Average optical density of BMP2 after PLS implantation ($n \geq 3$). (F) Average optical density of MGF in HUVECs ($n \geq 3$). (G) Average optical density of MGF in SMCs ($n \geq 3$). *$P < 0.05$, **$P < 0.01$, ***$P < 0.001$.

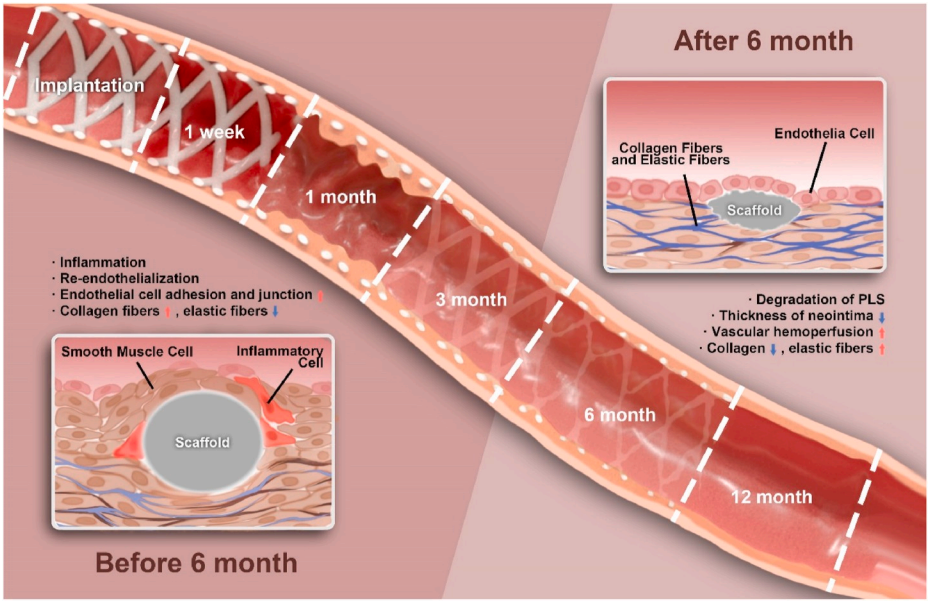

Fig. 10. "Two-processed remodeling" of vascular repair induced by PLS degradation. We proposed that vascular repair after PLS implantation can be divided into two different but connected processes: "0–6 months" (the injured blood vessels experienced vessel inflammation, neointima hyperplasia, and endothelial re-functionalization), and "after 6 months" (blood vessels experienced significant repair and vascular remodeling accompanying with PLS degradation). The key turn point revealed to be 6 months.

thrombus. Our results indicate that 6 months may be the key time point, as all vascular responses were continuous up to 6 months and blood vessels were completely transformed after 6 months, which included changes in the phenotype of cells and the components of the ECM. This phenomenon is also in line with the repair of vessels after injury. Vessels could respond to mechanical injury caused by balloon angioplasty and foreign body stimulation caused by PLS implantation and then undergo repair, whereas blood vessels could not enter the second stage of remodeling after BMS implantation. This phenomenon constitutes our theory of the "two-different remodeling processes" of vascular repair.

Together with the findings on the degradation of PLS, we speculate that PLS support is markedly decreased at 6 months post-implantation, the scaffold struts begin to disintegrate. This new understanding may be important in the optimization and clinical application of scaffolds in the future. To align degradation with vessel repair, improvements in base materials and architectural design will be needed in the future. Moreover, the sequential release of drugs and effective targeting design that are now popular in the field of drug delivery can also be applicable to PLS [57,58]. For instance, drugs with different therapeutic effects can be combined to meet the requirements of staged vascular repair. Anti-inflammatory, anti-proliferative, anti-thrombotic, and intimal function-promoting drug coatings can be applied during the 0–6 months [37,59,60], whereas the drug coatings promoting the positive phenotype of media cells and extracellular matrix repair can be applied after 6 months. The design of a coaxial drug coating, as previously reported by us, provides a means to achieve the staged release of drugs with different efficiencies [61]. Combining all these aforementioned parameters, the 3-D printing technology can be significantly improved for future clinical applications.

Although animals such as rats [26], rabbits [62], porcine [63] and monkeys [64,65] have been extensively used in previous studies it is of course preferable to apply PLS in an *in vivo* atherosclerosis animal model, for the application of endovascular stent is always in atherosclerosis vascular [66–69]. Additionally, atherosclerosis isn't an idiopathic disease for the rat. Furthermore, the degradation characteristic of PLS and vascular responses need to be observed in an animal with a longer life cycle to provide the possibility of observing full degradation of PLS, which would provide more useful information considering both application and technical improvement of PLS.

5. Conclusion

In conclusion, this study showed that vascular repair after BRS implantation involved two processes, "0–6 months" (characterized by inflammation, neointimal hyperplasia, and endothelial re-functionalization) and "after 6 months" (characterized by scaffold degradation and positive vascular remodeling), which were similar to the remodeling process after vascular injury. Despite the complex reactions that blood vessels experienced during the entire process, they regained their normal state after 6 months. In addition, our findings showed that vascular repair and remodeling aligned with the degradation of BRS, and endothelial barrier function was recovered and positive vascular remodeling was completed within 12 months. This study also provides new insights for the research of this 3-D printed BRS and new insights for the design of next generation PLS with sequential drug release coatings to accelerate vessel remodeling and to improve scaffold degradation and recovery. However, there are still limitations in current study, we couldn't ignore that we didn't observe fully degradation of PLS by using long life atherosclerosis model or apply CFD to show mechanical changes induced by complex degradation of PLS. And these limitations are going to overcome in our further research.

CRediT authorship contribution statement

Tieying Yin: Conceptualization, and experimental design, Writing – original draft, Funding acquisition, Supervision. **Ruolin Du:** the experiment investigation, Formal analysis, Writing – original draft. **Yang Wang:** the experiment investigation, Formal analysis, Writing – original draft. **Junyang Huang:** the experiment investigation. **Shuang Ge:** the experiment investigation. **Yuhua Huang:** the experiment investigation. **Youhua Tan:** Writing – review & editing. **Qing Liu:** Writing – review & editing. **Zhong Chen:** the radiographic data analysis. **Hanqing Feng:** the experiment investigation. **Jie Du:** Writing – review & editing. **Yazhou Wang:** Conceptualization, and experimental design, Writing – review & editing, Funding acquisition, Supervision. **Guixue Wang:** Conceptualization, and experimental design, Writing – review & editing, Funding acquisition, Supervision, All authors read and approved final manuscript..

Declaration of competing interest

The authors declare that they have no conflict of interest.

Acknowledgments

This research was supported by National Key R&D Program of China (2016YFC1102305); National Natural Science Foundation of China (12032007, 31971242); the Natural Science Foundation of Chongqing (cstc2019jcyj-msxmX0307, cstc2019jcyj-19zdxmX0009, cstc2019jcyj-zdxmX0028); the Fundamental Research Funds for the Central Universities (2019CDYGZD002, 2021CDJCGJ007). The authors would like to thank Dr. Xiaohui Zhao at Department of Cardiology, Second Affiliated Hospital of Army Medical University for his assistance of OCT experiments, Dr. Scott Richardson and Professor Xiaoyu Luo at University of Glasgow for their kind assistance of writing improvement. The authors also want to thank the support from the Chongqing Engineering Laboratory in Vascular Implants, the Public Experiment Center of State Bioindustrial Base (Chongqing).

Appendix A. Supplementary data

Supplementary data to this article can be found online at https://doi.org/10.1016/j.bioactmat.2021.08.020.

References

[1] H. Jinnouchi, S. Torii, A. Sakamoto, F.D. Kolodgie, R. Virmani, A.V. Finn, Fully bioresorbable vascular scaffolds: lessons learned and future directions, Nat. Rev. Cardiol. 16 (5) (2019) 286–304.

[2] Y. Onuma, P.W. Serruys, Bioresorbable scaffold: the advent of a new era in percutaneous coronary and peripheral revascularization? Circulation 123 (7) (2011) 779–797.

[3] A. Seth, Y. Onuma, R. Costa, P. Chandra, V.K. Bahl, C.N. Manjunath, A.U. Mahajan, V. Kumar, P.K. Goel, G.S. Wander, M.S. Kalarickal, U. Kaul, V.K.A. Kumar, P. C. Rath, V. Trehan, G. Sengottuvelu, S. Mishra, A. Abizaid, P.W. Serruys, First-in-human evaluation of a novel poly-l-lactide based sirolimus-eluting bioresorbable vascular scaffold for the treatment of de novo native coronary artery lesions: meres-1 trial, EuroIntervention 13 (4) (2017) 415–423.

[4] H. Nef, J. Wiebe, N. Boeder, O. Dörr, T. Bauer, K.E. Hauptmann, A. Latib, A. Colombo, D. Fischer, T. Rudolph, N. Foin, G. Richardt, C. Hamm, A multicenter post-marketing evaluation of the Elixir DESolve ® Novolimus-eluting bioresorbable coronary scaffold system: first results from the DESolve PMCF study, Catheter, Cardiovasc. Interv. 92 (6) (2018) 1021–1027.

[5] Y.L. Han, B. Xu, G.S. Fu, X.Z. Wang, K. Xu, C.Y. Jin, L. Tao, L. Li, Y.Q. Hou, X. Su, Q. Fang, L.L. Chen, H.L. Liu, B. Wang, Z.Y. Yuan, C.Y. Gao, S.H. Zhou, Z.W. Sun, Y. Y. Zhao, C.D. Guan, G.W. Stone, NeoVas Randomized Controlled Trial Investigators, Neovas randomized controlled trial investigators, a randomized trial comparing the neovas sirolimus-eluting bioresorbable scaffold and metallic everolimus-eluting stents, JACC Cardiovasc. Interv. 11 (3) (2018) 260–272.

[6] P.W. Serruys, B. Chevalier, D. Dudek, A. Cequier, D. Carrié, A. Iniguez, M. Dominici, R.J. van der Schaaf, M. Haude, L. Wasungu, S. Veldhof, L. Peng, P. Staehr, M.J. Grundeken, Y. Ishibashi, H.M. Garcia-Garcia, Y. Onuma, A bioresorbable everolimus-eluting scaffold versus a metallic everolimus-eluting stent for ischaemic heart disease caused by de-novo native coronary artery lesions (absorb II): an interim 1-year analysis of clinical and procedural secondary outcomes from a randomised controlled trial, Lancet 385 (9962) (2015) 43–54.

[7] G. Caiazzo, I.D. Kilic, E. Fabris, R. Serdoz, A. Mattesini, N. Foin, S. De Rosa, C. Indolfi, C. Di Mario, Absorb bioresorbable vascular scaffold: what have we learned after 5 years of clinical experience? Int. J. Cardiol. 201 (2015) 129–136.

[8] B. Chevalier, Y. Onuma, A.J. van Boven, J.J. Piek, M. Sabaté, S. Helqvist, A. Baumbach, P.C. Smits, R. Kumar, L. Wasungu, P.W. Serruys, Randomised comparison of a bioresorbable everolimus-eluting scaffold with a metallic everolimus-eluting stent for ischaemic heart disease caused by de novo native coronary artery lesions: the 2-year clinical outcomes of the absorb II trial, EuroIntervention 12 (9) (2016) 1102–1107.

[9] D.J. Kereiakes, S.G. Ellis, D.C. Metzger, R.P. Caputo, D.G. Rizik, P.S. Teirstein, M. R. Litt, A. Kini, A. Kabour, S.O. Marx, J.J. Popma, S.H. Tan, D.E. Ediebah, C. Simonton, G.W. Stone, ABSORB III Investigators, Absorb III investigators, clinical outcomes before and after complete everolimus-eluting bioresorbable scaffold resorption: five-year follow-up from the absorb III trial, Circulation 140 (23) (2019) 1895–1903.

[10] H. Jinnouchi, R. Virmani, A.V. Finn, Long-term vasomotion after absorb: fact or fiction? JACC Cardiovasc. Interv. 11 (16) (2018) 1572–1575.

[11] D.H. Zhu, I. Cockerill, Y.C. Su, Z.X. Zhang, J.Y. Fu, K.W. Lee, J. Ma, C. Okpokwasili, L.P. Tang, Y.F. Zheng, Y.X. Qin, Y.D. Wang, Mechanical strength, biodegradation, and in vitro and in vivo biocompatibility of Zn biomaterials, ACS Appl. Mater. Interfaces 11 (7) (2019) 6809–6819.

[12] H.T. Yang, C. Wang, C.Q. Liu, H.W. Chen, Y.F. Wu, J.T. Han, Z.C. Jia, W.J. Lin, D. Y. Zhang, W.T. Li, W. Yuan, H. Guo, H.F. Li, G.X. Yang, D.L. Kong, D.H. Zhu, K. Takashima, L.Q. Ruan, J.F. Nie, X. Li, Y.F. Zheng, Evolution of the degradation mechanism of pure zinc stent in the one-year study of rabbit abdominal aorta model, Biomaterials 145 (2017) 92–105.

[13] Y.Z. Wu, L. Shen, J.S. Yin, J.H. Chen, J.Y. Qian, L. Ge, J.B. Ge, XINSORB randomized clinical trial, Twelve-month angiographic and clinical outcomes of the xinsorb bioresorbable sirolimus-eluting scaffold and a metallic stent in patients with coronary artery disease, Int. J. Cardiol. 293 (2019) 61–66.

[14] Y.J. Zhang, X.Z. Wang, G.S. Fu, Q.M. Jing, G. Wang, C.Y. Jin, L.H. Xie, J.Z. Cai, B. Xu, Y.L. Han, Clinical and multimodality imaging results at 6 months of a bioresorbable sirolimus-eluting scaffold for patients with single de novo coronary artery lesions: the neovas first-in-man trial, EuroIntervention 12 (10) (2016) 1279–1287.

[15] T. Lhermusier, D. Carrie, G. Cayla, J. Fajadet, J. Sainsous, S. Elhadad, F. Tarragano, B. Chevalier, S. Ranc, C. Curinier, H. Le Breton, R. Koning, FRANCE ABSORB Investigators, Three-year clinical outcomes with the ABSORB bioresorbable vascular scaffold in real life: insights from the France ABSORB registry, Cathet. Cardiovasc. Interv. (2020) 1–9, https://doi.org/10.1002/ccd.29369.

[16] Y. Wu, Z. Yao, J. Yin, J. Chen, J. Qian, L. Shen, L. Ge, J.B. Ge, Three-year clinical outcomes of a sirolimus-eluting bioresorbable scaffold (XINSORB) and a metallic stent to treat coronary artery stenosis, Ann. Transl. Med. 22 (2020) 1489.

[17] Y. Wu, J. Yin, J. Chen, Z. Yao, J. Qian, L. Shen, L. Ge, J.B. Ge, Final report of the 5-year clinical outcomes of the XINSORB bioresorbable sirolimus-eluting scaffold in the treatment of single de novo coronary lesions in a first-in-human study, Ann. Transl. Med. 18 (2020) 1162.

[18] B. Zheng, M. Chen, X.G. Wang, B. Zhang, Q.P. Shi, Y. Huo, A novel three-dimensional printed sirolimus-eluting bioresorbable vascular scaffold evaluated by optical coherence tomography in a porcine model, Eur. Heart J. Suppl. 37 (2016) 1004.

[19] J. Zhao, Z.C. Mo, F.F. Guo, D.L. Shi, Q.Q. Han, Q. Liu, Drug loaded nanoparticle coating on totally bioresorbable PLLA stents to prevent in-stent restenosis, J. Biomed. Mater. Res. B Appl. Biomater. 106 (1) (2018) 88–95.

[20] S.H. Bradshaw, L. Kennedy, D.F. Dexter, J.P. Veinot, A practical method to rapidly dissolve metallic stents, Cardiovasc. Pathol. 18 (3) (2009) 127–133.

[21] Y.Z. Wu, L. Shen, Q.B. Wang, L. Ge, J. Xie, X. Hu, A.J. Sun, J.Y. Qian, J.B. Ge, Comparison of acute recoil between bioabsorbable poly-L-lactic acid XINSORB stent and metallic stent in porcine model, J. Biomed. Biotechnol. 2012 (2012) 413956.

[22] J.A. Ormiston, B. Webber, B. Ubod, O. Darremont, M.W. Webster, An independent bench comparison of two bioresorbable drug-eluting coronary scaffolds (Absorb and DESolve) with a durable metallic drug-eluting stent (ML8/Xpedition), EuroIntervention 11 (1) (2015) 60–67.

[23] Y.B. Fan, K.H. Xiu, H. Duan, M. Zhang, Biomechanical and histological evaluation of the application of biodegradable poly-L-lactic cushion to the plate internal fixation for bone fracture healing, Clin. Biomech. 23 (Suppl 1) (2008) S7–S16.

[24] D.Y. Zhao, T.T. Zhu, J. Li, L.G. Cui, Z.Y. Zhang, X.L. Zhuang, Poly(lactic- co-glycolic acid)-based composite bone-substitute materials, Bioact. Mater. 6 (2) (2020) 346–360.

[25] Z. Azhari, S. McMahon, L. Pierucci, W. Wang, R. Cameron, Short poly(ethylene glycol) block initiation of poly(l-lactide) di-block copolymers: a strategy for tuning the degradation of resorbable devices, Polym. Int. 67 (6) (2018) 726–738.

[26] W.H. Yan, T.H. Li, T.Y. Yin, Z.J. Hou, K. Qu, N. Wang, C. Durkan, L.Q. Dong, J. H. Qiu, H. Gregersen, G.X. Wang, M2 macrophage-derived exosomes promote the c-KIT phenotype of vascular smooth muscle cells during vascular tissue repair after intravascular stent implantation, Theranostics 10 (23) (2020) 10712–10728.

[27] T. Inoue, K. Croce, T. Morooka, M. Sakuma, K. Node, D.I. Simon, Vascular inflammation and repair: implications for re-endothelialization, restenosis, and stent thrombosis, JACC Cardiovasc. Interv. 4 (10) (2011) 1057–1066.

[28] J. Wiebe, H.M. Nef, C.W. Hamm, Current status of bioresorbable scaffolds in the treatment of coronary artery disease, J. Am. Coll. Cardiol. 64 (23) (2014) 2541–2551.

[29] S.J. Zhao, L.X. Gu, S.R. Froemming, On the importance of modeling stent procedure for predicting arterial mechanics, J. Biomech. Eng. 134 (12) (2012) 121005.

[30] K. Song, Y.Y. Bi, H.B. Zhao, T. Wu, F. Xu, G.Q. Zhao, Structural optimization and finite element analysis of poly-l-lactide acid coronary stent with improved radial strength and acute recoil rate, J. Biomed. Mater. Res. B Appl. Biomater. 108 (7) (2020) 2754–2764.

[31] R.W. Blair, N.J. Dunne, A.B. Lennon, G.H. Menary, Multi-objective optimisation of material properties and strut geometry for poly (L-lactic acid) coronary stents using response surface methodology, PloS One 14 (8) (2019), e0218768.

[32] F. Wajdi, A.E. Tontowi, I. Kusumaningtyas, A.R. Wijaya, Finite element investigation of GO reinforced PLLA stent deployment, in: 20181st International Conference on Bioinformatics, Biotechnology, and Biomedical Engineering - Bioinformatics and Biomedical Engineering, 2018, pp. 1–6.

[33] J.M. Jiménez, P.F. Davies, Hemodynamically driven stent strut design, Ann. Biomed. Eng. 37 (8) (2009) 1483–1494.

[34] D.A. Chistiakov, A.N. Orekhov, Y.V. Bobryshev, Endothelial barrier and its abnormalities in cardiovascular disease, Front. Physiol. 6 (2015) 365.

[35] M. Joner, G. Nakazawa, A.V. Finn, S.C. Quee, L. Coleman, E. Acampado, P. S. Wilson, K. Skorija, Q. Cheng, X. Xu, H.K. Gold, F.D. Kolodgie, R. Virmani, Endothelial cell recovery between comparator polymer-based drug-eluting stents, J. Am. Coll. Cardiol. 52 (5) (2008) 333–342.

[36] E. Harari, L. Guo, S.L. Smith, K.H. Paek, R. Fernandez, A. Sakamoto, H. Mori, M. D. Kutyna, A. Habib, S. Torii, A. Cornelissen, H. Jinnouchi, A. Gupta, F.D. Kolodgie, R. Virmani, A.V. Finn, Direct targeting of the mTOR (mammalian target of rapamycin) kinase improves endothelial permeability in drug-eluting stents-brief report, Arterioscler. Thromb. Vasc. Biol. 38 (9) (2018) 2217–2224.

[37] P. Majewska, E. Oledzka, M. Sobczak, Overview of the latest developments in the field of drug-eluting stent technology, Biomater. Sci. 8 (2) (2020) 544–551.

[38] D.C. Yang, W.H. Yan, J.H. Qiu, Y.H. Huang, T.H. Li, Y. Wang, Mussel adhesive protein fused with VE-cadherin extracellular domain promotes endothelial-cell tight junctions and *in vivo* endothelization recovery of vascular stent, J. Biomed. Mater. Res. B Appl. Biomater. 108 (1) (2020) 94–103.
[39] Y.P. Zhao, R.L. Du, T. Zhou, D.C. Yang, Y.H. Huang, Y. Wang, J.L. Huang, X.Y. Ma, F.G. He, J.H. Qiu, G.X. Wang, Arsenic trioxide-coated stent is an endothelium-friendly drug eluting stent, Adv. Healthc. Mater. 7 (15) (2018), e1800207.
[40] E. Dejana, E. Tournier-Lasserve, B.M. Weinstein, The control of vascular integrity by endothelial cell junctions: molecular basis and pathological implications, Dev. Cell 16 (2) (2009) 209–221.
[41] B.D. Cook, G. Ferrari, G. Pintucci, P. Mignatti, Tgf-β1 induces rearrangement of flk-1–ve-cadherin–β-catenin complex at the adherens junction through vegf-mediated signaling, J. Cell. Biochem. 105 (6) (2008) 1367–1373.
[42] N. Moriyama, K. Shishido, Y. Tanaka, S. Yokota, T. Hayashi, H. Miyashita, T. Koike, H. Yokoyama, T. Takada, T. Nishimoto, T. Ochiai, K. Tobita, F. Yamanaka, S. Mizuno, M. Murakami, S. Takahashi, S. Saito, Neoatherosclerosis 5 years after bioresorbable vascular scaffold implantation, J. Am. Coll. Cardiol. 71 (17) (2018) 1882–1893.
[43] L.N. Woodard, V.M. Page, K.T. Kmetz, M.A. Grunlan, Pcl-plla semi-ipn shape memory polymers (smps): degradation and mechanical properties, Macromol. Rapid Commun. 37 (23) (2016) 1972–1977.
[44] Y. Onuma, P.W. Serruys, T. Muramatsu, S. Nakatani, R.J. van Geuns, B. de Bruyne, D. Dudek, E. Christiansen, P.C. Smits, B. Chevalier, D. McClean, J. Koolen, S. Windecker, R. Whitbourn, I. Meredith, H.M. Garcia-Garcia, S. Veldhof, R. Rapoza, J.A. Ormiston, Incidence and imaging outcomes of acute scaffold disruption and late structural discontinuity after implantation of the absorb everolimus-eluting fully bioresorbable vascular scaffold: optical coherence tomography assessment in the absorb cohort b trial (a clinical evaluation of the bioabsorbable everolimus eluting coronary stent system in the treatment of patients with de novo native coronary artery lesions), JACC Cardiovasc. Interv. 7 (12) (2014) 1400–1411.
[45] T. Zhou, Y.M. Zheng, L. Sun, S.R. Badea, Y.H. Jin, Y. Liu, A.J. Rolfe, H.T. Sun, X. Wang, Z.J. Cheng, Z.S. Huang, N. Zhao, X. Sun, J.H. Li, J.Q. Fan, C. Lee, T. L. Megraw, W.T. Wu, G.X. Wang, Y. Ren, Microvascular endothelial cells engulf myelin debris and promote macrophage recruitment and fibrosis after neural injury, Nat. Neurosci. 22 (3) (2019) 421–435.
[46] H.I. Kim, K. Ishihara, S. Lee, J.H. Seo, H.Y. Kim, D. Suh, M.U. Kim, T. Konno, M. Takai, J.S. Seo, Tissue response to poly (l-lactic acid)-based blend with phospholipid polymer for biodegradable cardiovascular stents, Biomaterials 32 (9) (2011) 2241–2247.
[47] R.A. McDonald, C.A. Halliday, A.M. Miller, L.A. Diver, R.S. Dakin, J. Montgomery, M.W. McBride, S. Kennedy, J.D. McClure, K.E. Robertson, G. Douglas, K. M. Channon, K.G. Oldroyd, A.H. Baker, Reducing in-stent restenosis: therapeutic manipulation of mirna in vascular remodeling and inflammation, J. Am. Coll. Cardiol. 65 (21) (2015) 2314–2327.
[48] H.L. Xu, J.X. Jiang, W.Z. Chen, W.L. Li, Z.G. Chen, Vascular macrophages in atherosclerosis, J. Immunol. Res. (2019) 4354786.
[49] D.A. Chistiakov, I.A. Sobenin, A.N. Orekhov, Y.V. Bobryshev, Myeloid dendritic cells: development, functions, and role in atherosclerotic inflammation, Immunobiology 220 (6) (2015) 833–844.
[50] E.M. Conway, Thrombomodulin and its role in inflammation, Semin, Immunopathol 34 (1) (2012) 107–125.
[51] G. Tellides, J.S. Pober, Inflammatory and immune responses in the arterial media, Circ. Res. 116 (2) (2015) 312–322.
[52] L.S. Shankman, D. Gomez, O.A. Cherepanova, M. Salmon, G.F. Alencar, R. M. Haskins, P. Swiatlowska, A.A. Newman, E.S. Greene, A.C. Straub, B. Isakson, G. J. Randolph, G.K. Owens, Klf4-dependent phenotypic modulation of smooth muscle cells has a key role in atherosclerotic plaque pathogenesis, Nat. Med. 21 (6) (2015) 628–637.
[53] D. Milingos, H. Katopodis, S. Milingos, A. Protopapas, G. Creatsas, S. Michalas, A. Antsaklis, M. Koutsilieris, Insulin-like growth factor-1 isoform mrna expression in women with endometriosis: eutopic endometrium versus endometriotic cyst, Ann. N. Y. Acad. Sci. 1092 (2006) 434–439.
[54] A. Savvani, C. Petraki, P. Msaouel, E. Diamanti, I. Xoxakos, M. Koutsilieris, Igf-iec expression is associated with advanced clinical and pathological stage of prostate cancer, Anticancer Res. 33 (6) (2013) 2441–2445.
[55] L.A. Dyer, X. Pi, C. Patterson, The role of bmps in endothelial cell function and dysfunction, Trends. Endocrinol. Metab. 25 (9) (2014) 472–480.
[56] M.Y. Deng, Improving the osteogenic efficacy of bmp2 with mechano growth factor by regulating the signaling events in bmp pathway, Cell Tissue Res. 361 (3) (2015) 723–731.
[57] Y. Wang, K. Zhang, X. Qin, T.H. Li, J.H. Qiu, T.Y. Yin, J.L. Huang, S. McGinty, G. Pontrelli, J. Ren, Q.W. Wang, W. Wu, G.X. Wang, Biomimetic nanotherapies: red blood cell based core-shell structured nanocomplexes for atherosclerosis management, Adv. Sci. 6 (12) (2019) 1900172.
[58] Y. Yang, X.Y. Li, H. Qiu, P. Li, P.K. Qi, M.F. Maitz, T.X. You, R. Shen, Z.L. Yang, W. J. Tian, N. Huang, Polydopamine modified tio_2 nanotube arrays for long-term controlled elution of bivalirudin and improved hemocompatibility, ACS Appl. Mater. Interfaces 10 (9) (2018) 7649–7660.
[59] E. Lih, C.H. Kum, W. Park, S.Y. Chun, Y.J. Cho, Y.K. Joung, K.S. Park, Y.J. Hong, D. J. Ahn, B.S. Kim, T.G. Kwon, M.H. Jeong, J.A. Hubbell, D.K. Han, Modified magnesium mydroxide nanoparticles inhibit the inflammatory response to biodegradable poly(lactide-co-glycolide) implants, ACS Nano 12 (7) (2018) 6917–6925.
[60] Y.P. Zhao, G.C. Zang, T.Y. Yin, X.Y. Ma, L.F. Zhou, L.J. Wu, R. Daniel, Y.B. Wang, J. H. Qiu, G.X. Wang, A novel mechanism of inhibiting in-stent restenosis with arsenic trioxide drug-eluting stent: enhancing contractile phenotype of vascular smooth muscle cells via YAP pathway, Bioact. Mater. 6 (2) (2021) 375–385.
[61] R.L. Du, Y.Z. Wang, Y.H. Huang, Y.P. Zhao, D.C. Zhang, D.Y. Du, Y. Zhang, Z.G. Li, S. McGinty, G. Pontrelli, T.Y. Yin, G.X. Wang, Design and testing of hydrophobic core/hydrophilic shell nano/micro particles for drug-eluting stent coating, NPG Asia Mater. 10 (2018) 642–658.
[62] Z.J. Hou, W.H. Yan, T.H. Li, W. Wu, Y.L. Cui, X.J. Zhang, Y.P. Chen, T.Y. Yin, J. H. Qiu, G.X. Wang, Lactic acid-mediated endothelial to mesenchymal transition through TGF-β1 contributes to in-stent stenosis in poly-L-lactic acid stent, Int. J. Biol. Macromol. 155 (2020) 1589–1598.
[63] J. Iqbal, J. Chamberlain, S.E. Francis, J. Gunn, Role of animal models in coronary stenting, Ann. Biomed. Eng. 44 (2) (2016) 453–465.
[64] G.D. Curfman, S. Morrissey, J.A. Jarcho, J.M. Drazen, Drug-eluting coronary stents–promise and uncertainty, N, Engl. J. Med. 356 (10) (2007) 1059–1060.
[65] K. Egashira, K. Nakano, K. Ohtani, K. Funakoshi, G. Zhao, Y. Ihara, J. Koga, S. Kimura, R. Tominaga, K. Sunagawa, Local delivery of anti-monocyte chemoattractant protein-1 by gene-eluting stents attenuates in-stent stenosis in rabbits and monkeys, Arterioscler. Thromb. Vasc. Biol. 27 (12) (2007) 2563–2568.
[66] D. Wang, T. Deuse, M. Stubbendorff, E. Chernogubova, R.G. Erben, S.M. Eken, H. Jin, Y.H. Li, A. Busch, C.H. Heeger, B. Behnisch, H. Reichenspurner, R. C. Robbins, J.M. Spin, P.S. Tsao, S. Schrepfer, L. Maegdefessel, Local microRNA modulation using a novel anti-miR-21-eluting stent effectively prevents experimental in-stent restenosis, Arterioscler. Thromb. Vasc. Biol. 35 (9) (2015) 1945–1953.
[67] O. Masuo, T. Terada, G. Walker, M. Tsuura, K. Nakai, T. Itakura, Patency of perforating arteries after stent placement? A study using an in vivo experimental atherosclerosis-induced model, AJNR. Am. J. Neuroradiol. 26 (3) (2005) 543–548.
[68] F.A. Jaffer, M.A. Calfon, A. Rosenthal, G. Mallas, R.N. Razansky, A. Mauskapf, R. Weissleder, P. Libby, V. Ntziachristos, Two-dimensional intravascular near-infrared fluorescence molecular imaging of inflammation in atherosclerosis and stent-induced vascular injury, J. Am. Coll. Cardiol. 57 (25) (2011) 2516–2526.
[69] J.C. Palmaz, Balloon-expandable intravascular stent, AJR Am. J. Roentgenol. 150 (6) (1988) 1263–1269.